The Astrophysical Journal, 800:25 (23pp), 2015 February 10 doi:10.1088/0004-637X/800/1/25

CHEMICALLY DISTINCT NUCLEI AND OUTFLOWING SHOCKED MOLECULAR GAS IN Arp 220

R. Tunnard[1], T. R. Greve[1], S. Garcia-Burillo[2], J. Graciá Carpio[3], J. Fischer[4], A. Fuente[2], E. González-Alfonso[5], S. Hailey-Dunsheath[3], R. Neri[5], E. Sturm[3], A. Usero[2], and P. Planesas[2]
[1] Department of Physics and Astronomy, University College London, Gower Street, London WC1E 6BT, UK; richard.tunnard.13@ucl.ac.uk
[2] Observatorio Astronómico Nacional, Observatorio de Madrid, Alfonso XII, 3, E-28014 Madrid, Spain
[3] Max-Planck-Institute for Extraterrestrial Physics (MPE), Giessenbachstraße 1, D-85748 Garching, Germany
[4] Naval Research Laboratory, Remote Sensing Division, 4555 Overlook Ave SW, Washington, DC 20375, USA
[5] Universidad de Alcalá de Henares, Departamento de Física y Matemáticas, Campus Universitario, E-28871 Alcalá de Henares, Madrid, Spain
[6] IRAM, 300 rue de la Piscine, Domaine Universitaire, F-38406 Saint Martin d'Hères Cedex, France
Received 2014 August 20; accepted 2014 December 8; published 2015 February 5

ABSTRACT

We present the results of interferometric spectral line observations of Arp 220 at 3.5 mm and 1.2 mm from the Plateau de Bure Interferometer, imaging the two nuclear disks in $H^{13}CN$(1–0) and (3–2), $H^{13}CO^+$(1–0) and (3–2), and $HN^{13}C$(3–2) as well as SiO(2–1) and (6–5), $HC^{15}N$(3–2), and SO(6_6–5_5). The gas traced by SiO(6–5) has a complex and extended kinematic signature including a prominent P Cygni profile, almost identical to previous observations of HCO^+(3–2). Spatial offsets 0.″1 north and south of the continuum center in the emission and absorption of the SiO(6–5) P Cygni profile in the western nucleus (WN) imply a bipolar outflow, delineating the northern and southern edges of its disk and suggesting a disk radius of ∼40 pc, consistent with that found by ALMA observations of Arp 220. We address the blending of SiO(6–5) and $H^{13}CO^+$(3–2) by considering two limiting cases with regards to the $H^{13}CO^+$ emission throughout our analysis. Large velocity gradient modeling is used to constrain the physical conditions of the gas and to infer abundance ratios in the two nuclei. Our most conservative lower limit on the [$H^{13}CN$]/[$H^{13}CO^+$] abundance ratio is 11 in the WN, compared with 0.10 in the eastern nucleus (EN). Comparing these ratios to the literature we argue on chemical grounds for an energetically significant active galactic nucleus in the WN driving either X-ray or shock chemistry, and a dominant starburst in the EN.

Key words: galaxies: active – galaxies: individual (Arp 220) – galaxies: ISM – galaxies: jets – submillimeter: general

1. INTRODUCTION

Local ultra luminous infrared galaxies (ULIRGs; defined as $L_{8-1000\mu m} > 10^{12}\,L_\odot$) as revealed by *IRAS* (Soifer et al. 1987, see also Sanders & Mirabel 1996; Lonsdale et al. 2006) have been a topic of great interest since their discovery as they are the products of gas-rich major mergers with extreme dust obscurations, star formation rates (∼100 $M_\odot\,yr^{-1}$), and molecular gas masses relative to other populations in the local Universe.

Early suspicions that the majority of ULIRG luminosity (30%–100%) arises from extremely compact structures on the scale of 100–300 pc were confirmed by interferometric CO observations and high resolution mid-IR imaging (e.g., Downes & Solomon 1998; Soifer et al. 2000), as well as from the analysis of molecular absorption lines in the far-IR (González-Alfonso et al. 2012, and references therein, hereafter GA12). In many cases this compact source is found to be a dust enshrouded active galactic nuclei (AGNs; e.g., Soifer et al. 1999; Lonsdale et al. 2006). Indeed, in Seyfert I type ULIRGs the AGN contribution to the bolometric luminosity can be as high as 75% (Veilleux et al. 2009). AGNs have been known for some time to play a pivotal role in galaxy evolution from the observed correlation between the mass of the central supermassive black hole and that of its host spheroid (Magorrian et al. 1998; Ferrarese & Merritt 2000; Tremaine et al. 2002). AGN feedback is thought to be responsible for the observed sharp cutoff at the upper end of the galactic mass function (Silk & Rees 1998). While AGNs provide an excess of energy for quenching star formation (∼80× the gravitational binding energy of their host galaxies; Fabian 2012), it is uncertain how this energy is coupled to the interstellar medium (ISM) and surrounding dust, and in particular whether there is sufficient momentum coupling to evacuate the central regions of gas. Nevertheless, massive molecular outflows from AGNs residing in local ULIRGs have recently been observed, (Cicone et al. 2014, and references therein), while ionized outflows have been found to be not only ubiquitous, but to exist with sufficient outflow rates to shape galaxy evolution (Harrison et al. 2014). These results have confirmed that AGNs can drive outflows in excess of the host starburst, but that frequently most of the mass in these outflows is moving slower than escape velocity, perhaps leading to future bursts of star formation as the gas fountains back into the host. Feedback from star formation in the form of stellar winds and supernovae also has a significant role to play in galaxy evolution, although this is predominantly in low mass galaxies where it is responsible for the low-mass turnover in the galactic mass function. Nevertheless, it may significantly contribute to feedback and outflows in massive galaxies by heating of the ISM (Efstathiou 2000).

The prototypical ULIRG Arp 220 ($z = 0.01818$) has been extensively studied across the entire EM-spectrum, revealing an extraordinarily dense and massive galactic merger (Soifer et al. 1984; Emerson et al. 1984; Young et al. 1984; Scoville et al. 1991; McDowell et al. 2003). It is a late-stage merger with two high column density ($N_{H_2} \gtrsim 1 \times 10^{25}\,cm^{-2}$), counter-rotating disks (separation ≃400 pc along the east-west axis) orbiting within a much larger gas disk (radius ≃ 0.25–1.5 kpc, average molecular gas density ∼ $10^3\,cm^{-3}$), potentially with an extended galactic halo (Sakamoto & Scoville 1999; Mundell et al. 2001; Sakamoto et al. 2008; Engel et al. 2011; González-Alfonso et al. 2012). Arp 220 is extremely dusty with $A_V > 1000$ mag toward the central nuclear region

(Fischer et al. 1997), and possesses at least three distinct stellar populations: a 10 Myr old starburst, a $\gtrsim$1 Gyr old population and a nascent, $\lesssim$7 Myr old non-starburst component, all distributed across the kiloparsec scale merger (Wilson et al. 2006; Rodríguez Zaurín et al. 2008; Engel et al. 2011).

There is mounting evidence for an AGN in the western nucleus (WN) of Arp 220 (Downes & Eckart 2007, and references therein) as well as a nuclear starburst revealed with very long baseline interferometry (Rodríguez Zaurín et al. 2008; Batejat et al. 2011). In particular, the mass, luminosity and dust temperatures have previously been used in attempts to identify an AGN. Sakamoto et al. (2008) and Engel et al. (2011) found dynamical masses in the WN and EN from CO and stellar kinematics respectively. Within 100 pc of the continuum centers of each nuclei they agree that the masses are on the order of $\sim 1 \times 10^9\,M_\odot$, although Engel et al. (2011) found masses closer to $\sim 5 \times 10^9\,M_\odot$. When Wilson et al. (2014) combined these results with their own high resolution ALMA observations of the nuclear continua, they obtained luminosity-mass ratios $540\,L_\odot\,M_\odot^{-1}$ and $30\,L_\odot\,M_\odot^{-1}$ for the WN and EN respectively: they conclude that the high WN ratio could be an AGN, or a hot starburst. Dust temperatures in the WN have been found from millimetre continuum measurements to be ~180–200 K, once accounting for optical depth effects (Downes & Eckart 2007; Wilson et al. 2014), while far-IR absorption lines suggest temperatures as high as 400 K (GA12). Such temperatures are usually associated with dusty toroids around AGNs (e.g., Weiß et al. 2007). Attempts to identify an AGN from X-ray observations have also been unsuccessful, but due to the Compton thick H_2 column density ($\sim 1 \times 10^{25}$ cm^{-2}) toward the WN any X-ray emission would be almost completely attenuated (Wilson et al. 2014). Molecular outflows have been observed in OH^+, H_2O^+ and H_2O by Rangwala et al. (2011); González-Alfonso et al. (2012) and in CO(3–2), HCO^+(4–3) and (3–2) by Sakamoto et al. (2009, hereafter Sa09), although these could be driven by either an AGN or a starburst. Mangum et al. (2013) confirmed a hot, dense gas phase through NH_3 thermometry, finding solutions including $T_k \sim 300$ K at $n_{H_2} \sim 10^6$ cm^{-3}.

Sa09 observed the HCO^+(3–2), (4–3) and CO(3–2) lines at high resolution (~0.″3) with the Sub-Millimetre Array (SMA), identifying prominent P Cygni profiles in both nuclei in the HCO^+ lines as well as absorption about the CO(3–2) line center. All of their WN lines displayed redshifted emission out to +500 km s^{-1}, while the HCO^+ lines showed maximum absorption around -100 km s^{-1}, but with some signs of blueshifted absorption out to -500 km s^{-1}, mixed with some blueshifted emission. The HCO^+(4–3) lines in both nuclei presented much cleaner P Cygni profiles than the (3–2) lines, although they still showed extended redward emission.

The warm, dense dust in the WN (Sa09 found $T_d \simeq 130$ K, Matsushita et al. 2009 suggested T_d could be as high as 310 K and optically thick at 435 μm while GA12 found $T_d \simeq 90$–120 K and that the dust could be optically thick out to 2.4 mm) provides a powerful radiation source against which absorption in molecular outflows can be clearly seen. In particular Sa09 and Papadopoulos et al. (2010) noted that the unusually high dust temperature favors the observation of higher frequency rotational transitions in absorption, and in the case of CO(6–5) Papadopoulos et al. (2010) found that the optical thickness of the dust in Arp 220 suppresses emission in higher transitions.

In this work, we present a P Cygni profile in SiO(6–5) toward the western nucleus (WN) of Arp 220. We also report the Plateau de Bure Interferometer (PdBI) observations of SiO(2–1), $H^{13}CN$ and $H^{13}CO^+$ (3–2) and (1–0); $HN^{13}C$ and $HC^{15}N$ (3–2) and SO(6_6–5_5). The lower optical depths of the ^{13}C isotopologues provide a better measure of abundances than the ^{12}C isotopologues, while the millimetre observations allow us to see through much of the dust enshrouding the nuclear disks of Arp 220. This combination of effects allows us to probe deeper into the driving regions of Arp 220 than has previously been possible. The observations are outlined in Section 2 and the continuum and line identification are discussed in Section 3. We outline the details of the lines in each nuclei in Sections 4 and 5, before entering into a more complete analysis in Section 6. Finally we discuss the significance of our results in Section 7.

We assume a flat universe with the 2013 Planck cosmological parameters (Planck Collaboration et al. 2013): $h = 0.673$, $\Omega_m = 0.315$ and $\Omega_\Lambda = 0.685$. For Arp 220 at $z_{co} = 0.01818$ (V_{co}(WN) $= 5355 \pm 15$ km s^{-1}, V_{co}(EN) $= 5415 \pm 15$ km s^{-1}, radio, LSR, Sa09) this gives a scale of 384 pc/″ and a luminosity distance $D_L = 82.1$ Mpc (Wright 2006). Our longest baseline for the 1.2 mm data was 382.5 kilowavelengths and 218.1 kilowavelengths at 3.5 mm, giving a maximum resolution ≃0.″37, or ~140 pc at 1.2 mm and ≃0.″70, or ~270 pc at 3.5 mm.

2. OBSERVATIONS AND DATA REDUCTION

We obtained two data sets from the IRAM PdBI at 3.5 mm (2007 February 1 and 2007 March 14 in the A configuration (beam 1.″44 × 0.″70, PA = 22°, maximum angular scale ~5.″7)) and one at 1.2 mm (2011 January 11 in the B configuration (beam 0.″52 × 0.″37, PA = 44°, maximum angular scale ~9.″1)). All six antennas were available for all observations. Total on source time for 3.5 mm was 17550 s and 21690 s for 1.2 mm.

For both 2007 observations the bandpass was classed as excellent, with excellent and good amplitude calibrations in the February and March observations respectively. The correlator was centered on 85.0474 GHz sky frequency, corresponding to 85.2783 GHz in the $z_{co} = 0.01818$ rest frame, and had a bandwidth of 965 MHz. Bandpass calibrators were 3C273 and 3C454.3, amplitude and phase calibration used 1611+343 and radio seeing was 0.″30. The data were reduced in CLIC, and the UV tables produced were analyzed and mapped using the MAPPING program in the IRAM proprietary software GILDAS[7] (Guilloteau & Lucas 2000). These observations targeted SiO(2–1), $H^{13}CN$(1–0) and $H^{13}CO^+$(1–0) in both nuclei.

The 1.2 mm data used the full 3.6 GHz bandwidth of the WideX correlator, centered on 255.127 GHz sky frequency, corresponding to 259.765 GHz in the $z_{co} = 0.01818$ rest frame, with spectral channels of width 3.9 MHz (~4.59 km s^{-1}), with the aim of mapping $H^{13}CN$(3–2), $H^{13}CO^+$(3–2) and SiO(6–5). The observations were phase centered at R.A.: $15^h34^m57^s24$, Decl.: 23°30′11″.2. The data were imaged from UV tables using natural weighting.

For both frequencies we estimate a 10% uncertainty in the absolute flux calibration. The Hogbom CLEAN algorithm (Högbom 1974) was used to produce data cubes, cleaning down to a flux level of ~0.5 σ. We obtain rms. noise levels of 3.3 mJy beam^{-1} at 1.2 mm with channels of 4.59 km s^{-1} and 1.60 mJy beam^{-1} at 3.5 mm with channels of 8.81 km s^{-1}.

[7] http://www.iram.fr/IRAMFR/GILDAS

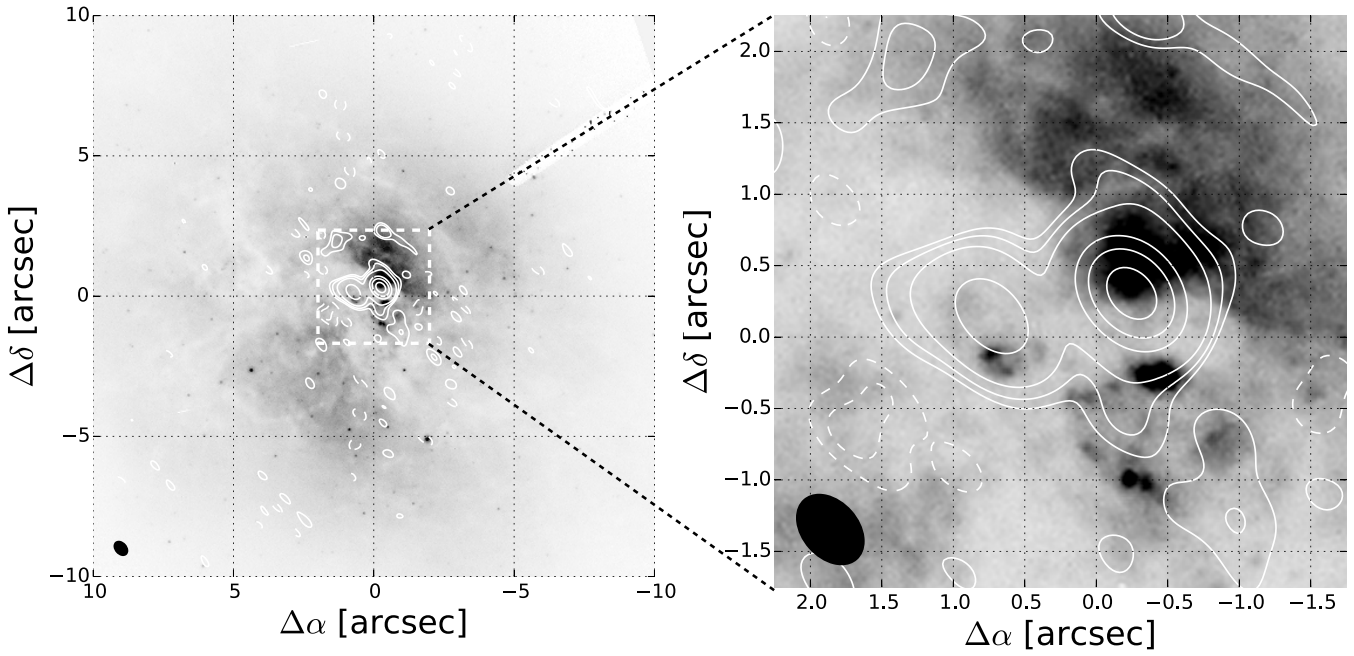

Figure 1. *Hubble Space Telescope* (*HST*) ACS/HRC F814W (F814W is an *HST* wideband filter centered on 814 nm covering the *I* band) image with the 1.2 mm continuum contours overlaid. The compact red emission demonstrates the highly obscured nature of the central regions of Arp 220. The right hand image shows a $4'' \times 4''$ extract centering on the millimetre continua. The 1.2 mm continuum contours (in white) are overlaid at −5, −3, 3, 5, 10, 50, 100, 200 and 300σ and the 1.2 mm beam ($0\farcs52 \times 0\farcs37$) is shown in the bottom left hand corners. The *HST* image was created with the help of the ESA/ESO/NASA FITS Liberator, and has a nominal astrometric accuracy of $0\farcs3$.

3. RESULTS

3.1. Continuum

Interpretation of the line profiles and implied kinematics requires knowledge of the dust properties of the source, and in particular to what extent dust is obscuring our observations. The continuum emission is dominated by dust, so provides a means of studying the dust properties in Arp 220. Furthermore, we must confirm that our detected continuum is consistent with previous observations to ensure that the sub-continuum absorption is real. The continuum analysis is summarized below, and additional details are included in Appendix A.

The 1.2 mm continuum was obtained from the central 443 km s^{-1} wide line free region from 259.388–259.765 GHz, WN rest frame, and the 3.5 mm continuum was found from the central 511 km s^{-1} wide line free region from 85.925–86.623 GHz, WN rest frame. These regions are line free in both nuclei. Continuum contours for the 1.2 mm nuclei are shown in Figure 1. The two nuclei are at best marginally resolved, so we worked in the UV plane to constrain the continuum parameters of the two nuclei. Fitting elliptical Gaussians with the GILDAS task UV_FIT we found 1.2 mm continuum centers and sizes, and fluxes (R.A. = $15^{h}34^{m}57^{s}220$, Decl. = $23^{\circ}30'11''50$, FWHM = $0\farcs19 \times 0\farcs15$, $S_{1.2\,mm} = 200 \pm 20$ mJy and $S_{3.5\,mm} = 17 \pm 2$ mJy for the WN and R.A. = $15^{h}34^{m}57^{s}291$, Decl. = $23^{\circ}30'11''34$, FWHM = $0\farcs26 \times 0\farcs18$, $S_{1.2\,mm} = 71 \pm 7$ mJy and $S_{3.5\,mm} = 11 \pm 1$ mJy for the EN). These results and comparable measurements from the literature are included in Appendix A (Table 7). Our fitted continuum centers at 1.2 mm are precisely in agreement with those that Wilson et al. (2014) found at much higher resolution ($0\farcs363 \times 0\farcs199$) with ALMA. Our 1.2 mm flux densities are consistent with the 1.1 mm flux densities of Sa09 who found 200 mJy and 70 mJy with 15% uncertainties. Subtracting synchrotron emission we find flux densities 196 ± 20 mJy and 69 ± 7 mJy for the WN and EN at 1.2 mm and 8 ± 2 mJy and 6 ± 1 mJy for the WN and EN at 3.5 mm.

The global (i.e., WN and EN, combined) dust optical depth and spectral index found from spectral energy distribution (SED) fitting of our continuum measurements and data from the literature were $\tau_{258GHz} = 0.06$ and $\beta = 1.5$, with a turnover frequency ∼1600 GHz. This is similar to the global fit of Rangwala et al. (2011), who found a turnover frequency of 1277 GHz and $\beta = 1.8$. However, compared with the four component SED fits of GA12, who for $\beta_{WN} = 1$–2 predict $\tau_{258GHz} = 2$–0.4 and $\tau_{86GHz} = 0.7$–0.04 in the WN, our value is low, most likely due to fitting only two components (GA12 used four). Due to the more sophisticated modeling of GA12 we use their dust optical depths.

3.2. Line Identification

Within the bandwidth of the WideX correlator we detected a plethora of wide, high signal-to-noise (S/N) lines in emission toward both nuclei of Arp 220, the frequencies and upper level energies of which are given in Table 1. The continuum subtracted spectra, including the multiple component Gaussian line fits, are shown in Figures 2–5. The fitting derived line parameters are given in Table 2, and an outline of the fitting procedure, including a full list of the fitted components, is included in Appendix B.

Lines were identified using the Cologne Database for Molecular Spectroscopy (CDMS; Müller et al. 2005) and the Spectral Line Atlas of Interstellar Molecules (SLAIM; Remijan et al. 2007), as well as the SMA line survey of Martín et al. (2011). Our final line list consists of $H^{13}CN$(1–0) and (3–2), $HN^{13}C$(3–2), SiO(2–1) and (6–5), $H^{13}CO^{+}$(1–0) and (3–2), SO(6_6–5_5) and $HC^{15}N$(3–2). The WN $HN^{13}C$(3–2) line extends beyond the end of our spectrum. We see the blue edge of what is likely the SO(2_2–1_1) in the 3.5 mm spectra, but almost the entire line is beyond the red edge of the spectrum. The relative contributions of

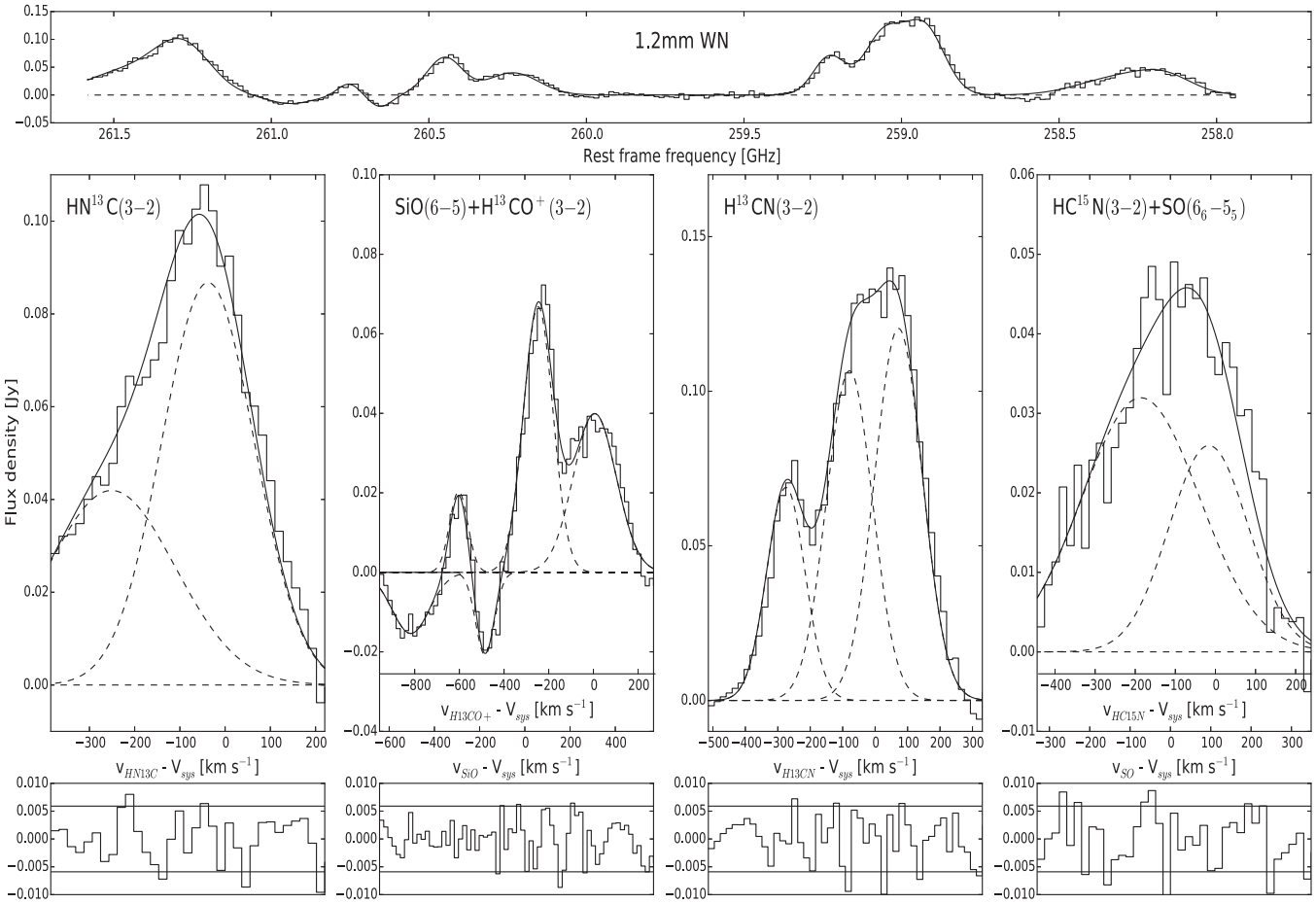

Figure 2. Continuum subtracted spectrum of Arp 220 WN extracted using 1″ diameter circular apertures centered on the continuum center. Top: the whole spectrum with the fitted lines overlaid. Frequencies are rest frame with $z = 0.01818$. Middle: multiple component Gaussian fits to the observed lines, with velocities shown relative to the line centers. Bottom: residuals from the fitting. The horizontal lines indicate the $\pm 1\sigma$ rms. noise level (5.9 mJy). Reduced χ^2 values range from 0.25 to 0.7. Full details of fitting components are included in Appendix B.

Table 1
Observed Lines

Line	ν^a (GHz)	E_u/k (K)
$H^{13}CN(1–0)$	86.340	4.1
$H^{13}CO^+(1–0)$	86.754	4.2
SiO(2–1)	86.847	6.3
$HC^{15}N(3–2)$	258.157	24.8
$SO(6_6–5_5)$	258.256	56.5
$H^{13}CN(3–2)$	259.012	24.9
$H^{13}CO^+(3–2)$	260.255	25.0
SiO(6–5)	260.518	43.8
$HN^{13}C(3–2)$	261.263	25.1

Note. Rest frame frequency.

$SO(6_6–5_5)$ and $HC^{15}N(3–2)$ in the 1.2 mm spectrum are highly uncertain.

Vibrationally excited molecular absorption and emission (including HCN) was detected in Arp 220 by Salter et al. (2008) and Martín et al. (2011) respectively, suggesting that we may have some contribution from the vibrationally excited $H^{13}CN(v_2 = 1, J = 3–2, l = 1e \text{ and } 1f)$ lines at 258.936 GHz and 260.225 GHz respectively. However, the ratios of the predicted line intensities for the $v_2 = 0$ to $v_2 = 1$ transitions at 75 K and 300 K from the CDMS database (Müller et al. 2005) are $1 : 10^{-6}$ and $1 : 35$ respectively. This suggests that even with considerable mid-IR pumping (Aalto et al. 2007; Sakamoto et al. 2010; Rangwala et al. 2011) the vibrational lines should be below our noise level. Whether the effect of mid-IR pumping on the $v_{1,2} = 0$ rotational transitions is significant is still unclear (Rangwala et al. 2011; González-Alfonso et al. 2012).

3.2.1. SiO and $H^{13}CO^+$

There is significant uncertainty regarding the identification of SiO and $H^{13}CO^+$ in our spectra. At both observing frequencies and in both nuclei there is the possibility that all of the line components shown in the SiO+$H^{13}CO^+$ boxes in Figures 2–5 are due to SiO, with no significant $H^{13}CO^+$ detection. Therefore, we examine the kinematic, spatial and line brightness evidence in an attempt to constrain the contribution of $H^{13}CO^+$ at 3.5 mm and at 1.2 mm. While Sa09 provide a comprehensive benchmark with their $HCO^+(3–2)$ observations there are no published observations of $HCO^+(1–0)$ in Arp 220, so that the following analysis of $H^{13}CO^+$ contribution focuses on the (3–2) transition in the 1.2 mm data.

Kinematically, a comparison with the $HCO^+(3–2)$ spectra of Sa09, shown in Figure 6, reveals startlingly similarities between the line profiles of their $HCO^+(3–2)$ and those of our SiO(6–5)–$H^{13}CO^+(3–2)$ line complex, in both nuclei. Particularly in the WN, the line profiles are extremely similar, with all five of our fitted Gaussian line components in Figure 2

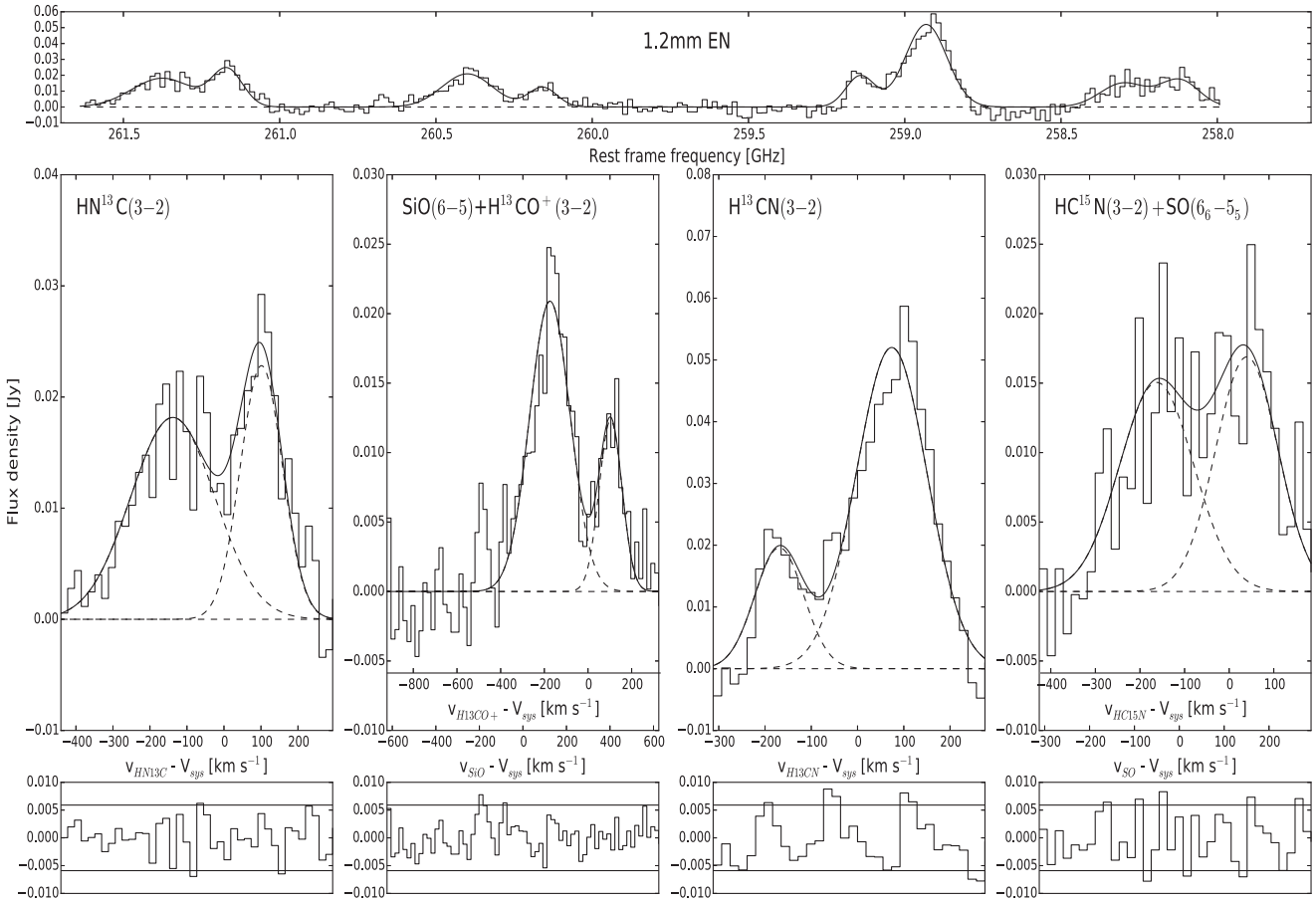

Figure 3. Continuum subtracted spectrum of Arp 220 EN extracted using 1″ diameter circular apertures centered on the continuum center. Top: the whole spectrum with the fitted lines overlaid. Frequencies are rest frame with $z = 0.01839$. Middle: multiple component Gaussian fits to the observed lines, with velocities shown relative to the line centers. Bottom: residuals from the fitting. The horizontal lines indicate the $\pm 1\sigma$ rms. noise level (5.9 mJy). Reduced χ^2 values range from 0.25 to 0.7. Full details of fitting components are included in Appendix B.

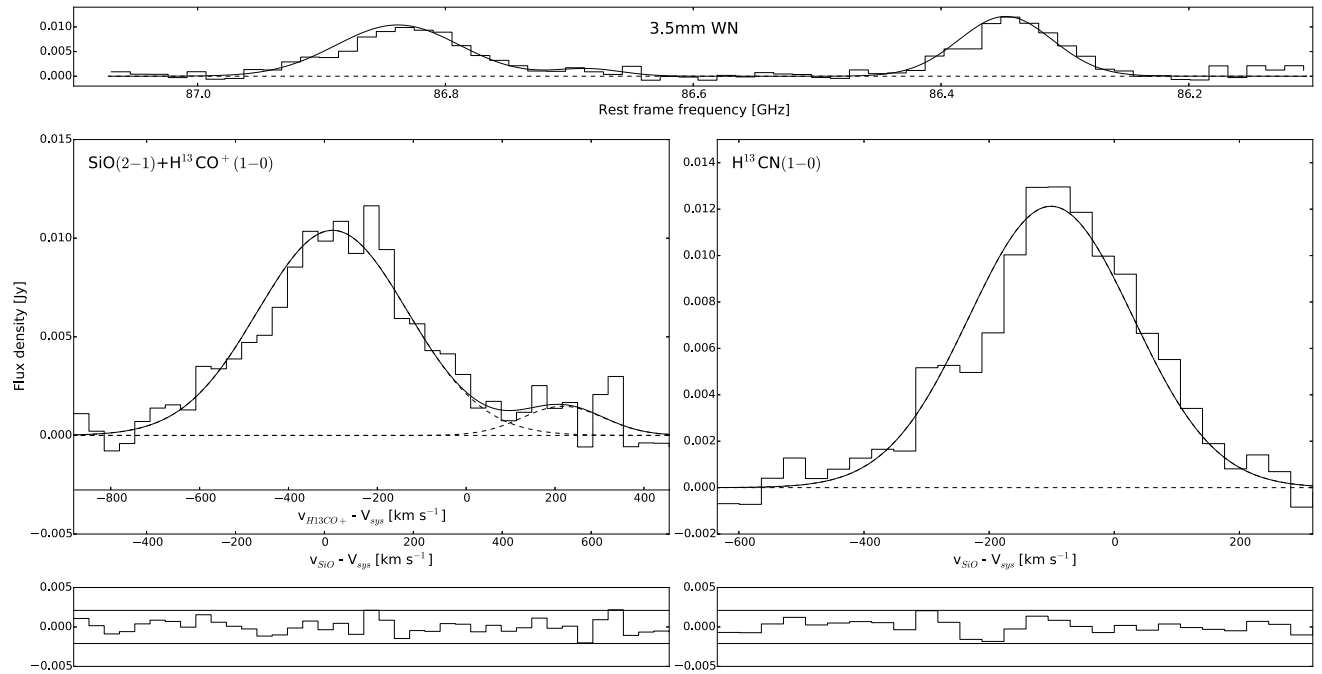

Figure 4. Continuum subtracted spectrum of Arp 220 WN extracted using elliptical apertures with major and minor axes equal to scaled FWHMs of our 3.5 mm beam, centered so as to minimize inter-nuclear contamination (R.A.: $15^{h}34^{m}57^{s}226$, Decl.: $23^{\circ}30'11''613$, scaling = 1.8). Top: the whole spectrum with the fitted lines overlaid. Frequencies are rest frame with $z = 0.01818$. Middle: multiple component Gaussian fits to the observed lines, with velocities shown relative to the line centers. Bottom: residuals from the fitting. The horizontal lines indicate the $\pm 1\sigma$ rms. noise level (2.1 mJy). Reduced χ^2 values range from 0.4 to 0.5. Full details of fitting components are included in Appendix B.

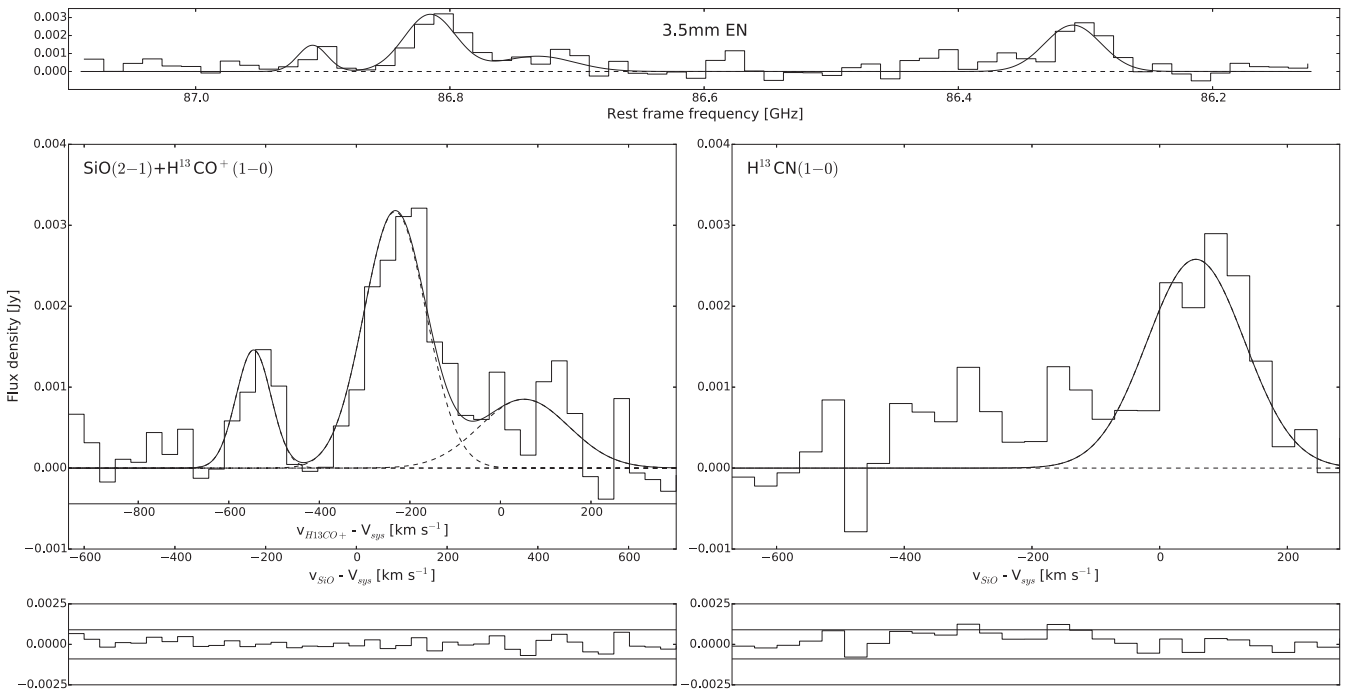

Figure 5. Continuum subtracted spectrum of Arp 220 EN extracted using elliptical apertures with major and minor axes equal to scaled FWHMs of our 3.5 mm beam, centered so as to minimize inter-nuclear contamination (R.A.: $15^{h}34^{m}57^{s}302$, Decl.: $23°30'11''415$, scaling = 1.2). Top: the whole spectrum with the fitted lines overlaid. Frequencies are rest frame with $z = 0.01839$. Middle: multiple component Gaussian fits to the observed lines, with velocities shown relative to the line centers. Bottom: residuals from the fitting. The horizontal lines indicate the $\pm 1\sigma$ rms. noise level (0.9 mJy). Reduced χ^2 values range from 0.2 to 0.5. Full details of fitting components are included in Appendix B.

having an equivalent in the HCO^+(3–2) spectrum. We rule out that the lines are entirely $H^{13}CO^+$(3–2) based on the significant ($\sim$320 km s^{-1}) velocity offset from the observed systemic velocity that this would require, but the kinematics cannot exclude the possibility that the lines are entirely SiO(6–5).

In our 3.5 mm spectra there are $\sim 1\sigma$ fitted components, currently attributed to $H^{13}CO^+$(1–0) (line center +250 km s^{-1} in the WN and line center +50 km s^{-1} in the EN, see Figures 4 and 5). Given the low significance of these components, as well as their considerable offset from their line centers, it is highly uncertain whether they are (1) real detections and (2) not an extended red component of the SiO(2–1) lines.

To search for spatial clues we produced line integrated velocity maps for all of our lines. Shown in Figure 7, we see that all of the 1.2 mm lines except for $H^{13}CO^+$(3–2) and SiO(6–5) are tightly bound around the nuclear continua, while the SiO(6–5)–$H^{13}CO^+$(3–2) line complex is strongly asymmetric about the WN continuum center, highlighting it as a line of interest. The 3.5 mm lines are observed at too low a spatial resolution for us to derive any solid conclusions on the spatial distribution of the emission. Spatially, Sa09 found the line integrated HCO^+(3–2) emission to be tightly collocated with the continuum emission, just as we see for our $H^{13}CN$(3–2) and $HN^{13}C$(3–2) lines, but contrary to what we see for the SiO(6–5)−$H^{13}CO^+$(3–2) line complex, which in the WN is offset north of the continuum center (Figure 7). While it is not impossible that $H^{13}CO^+$(3–2) is tracing very different regions from HCO^+(3–2), possibly due to optical depth effects, it is far more likely, especially in light of the kinematic evidence presented above, that the explanation for this unique spatial arrangement is that the line integrated emission is dominated by SiO(6–5).

As well as the kinematic and spatial comparisons discussed above, we also consider the brightness temperature ratios implied with detection and non-detection of $H^{13}CO^+$, using simple LTE estimations and HCO^+(3–2) data from Sa09 to identify whether non-detections of $H^{13}CO^+$(3–2) are physically viable. Details of the calculations are included in Appendix C. Sa09 report peak HCO^+(3–2) $T_B \sim 20$ K, with nuclear averaged values closer to 13.5 K for the WN and 10 K for the EN. Assuming that the component centered on the $H^{13}CO^+$(3–2) line center in Figure 2 is entirely $H^{13}CO^+$(3–2), we have corresponding temperatures of 2.5 K and 1 K in the WN and EN respectively, giving T_B ratios in the WN between 8 and 13.5. Assuming a $[^{12}C]/[^{13}C]$ abundance ratio of 60 (e.g., Langer & Penzias 1993), we find a minimum optical depth $\tau_{12} \geqslant 4.5$ (with $\tau_{13} \ll 1$), where τ_{12} and τ_{13} denote the optical depths of the ^{12}C and ^{13}C HCO^+(3–2)

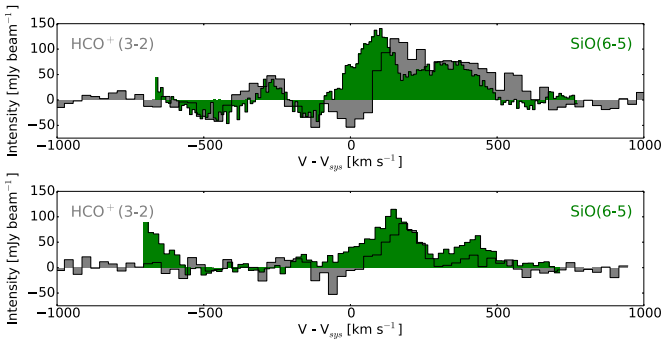

Figure 6. HCO^+(3–2) spectra from Sa09, with our SiO(6–5)-$H^{13}CO^+$(3–2) spectra scaled by a factor of 8 and overlaid. The WN lines (top) are centered on V_{sys}(WN) = 5355 km s^{-1}, the EN (bottom) on V_{sys}(EN) = 5415 km s^{-1}. The similarity between the profiles, in particular in the WN, suggests that our spectrum may be predominantly SiO(6–5), with no more than a minor contribution from the blended $H^{13}CO^+$(3–2) component at +317 km s^{-1}. The $H^{13}CO^+$(3–2) line center is +317 km s^{-1} redward of SiO(6–5), so cannot be the dominant contributor given the HCO^+(3–2) profile.

Table 2
Line Parameters in the Two Nuclei of Arp 220

Line	Flux[a] (Jy km s^{-1})	L'[b] (10^8 K km s^{-1} pc^2)	$T_{B,peak}$[c] (K)	FWZI (km s^{-1})	FWHM[d] (km s^{-1})
WN: R.A. 15:34:57.220, Decl. 23:30:11.50					
$H^{13}CN(3–2)$	52 ± 5	1.66 ± 0.24	11.2 ± 1.1	775 ± 25	464 ± 5
$H^{13}CN(1–0)$	4.0 ± 0.4	1.15 ± 0.12	1.94 ± 0.22	800 ± 50	285 ± 27
$HC^{15}N(3–2)$	6 ± 14	0.2 ± 0.5	1.86 ± 0.28	...	220 ± 40
$SO(6_6–5_5)$	12 ± 16	0.4 ± 0.6	2.8 ± 0.4	...	320 ± 270
SiO(6–5)[e]	17.1 ± 2.5	0.54 ± 0.08	5.75 ± 0.61	1200 ± 100	730 ± 30
SiO(6–5)[f]	7.6 ± 2.0	0.24 ± 0.06	5.75 ± 0.61	950 ± 50	...
SiO(2–1)[e]	4.8 ± 0.5	1.38 ± 0.14	1.62 ± 0.20	803 ± 22	440 ± 50
SiO(2–1)[f]	4.5 ± 0.5	1.28 ± 0.13	1.62 ± 0.20	...	370 ± 40
$H^{13}CO^+(3–2)$[f]	9.5 ± 1.1	0.30 ± 0.03	2.77 ± 0.29	500 ± 50	205 ± 21
$H^{13}CO^+(1–0)$[f]	0.35 ± 0.08	0.100 ± 0.022	0.22 ± 0.11	350 ± 50	200 ± 200
$HN^{13}C(3–2)$	37 ± 4	1.16 ± 0.13	7.72 ± 0.80	...	350 ± 100
EN: R.A. 15:34:57.291, Decl. 23:30:11.34					
Line	Flux[a] (Jy km s^{-1})	L'[b] (10^8 K km s^{-1} pc^2)	$T_{B,peak}$[c] (K)	FWZI (km s^{-1})	FWHM[d] (km s^{-1})
$H^{13}CN(3–2)$	12.7 ± 1.3	0.41 ± 0.04	4.91 ± 0.53	550 ± 50	523 ± 10
$H^{13}CN(1–0)$	0.50 ± 0.05	0.144 ± 0.015	0.57 ± 0.12	450 ± 100	170 ± 40
$HC^{15}N(3–2)$	3.1 ± 1.2	0.10 ± 0.04	1.50 ± 0.26	...	160 ± 60
$SO(6_6–5_5)$	3.2 ± 1.1	0.10 ± 0.04	1.10 ± 0.24	...	186 ± 26
SiO(6–5)[e]	6.5 ± 0.7	0.206 ± 0.029	2.48 ± 0.33	740 ± 80	410 ± 20
SiO(6–5)[f]	4.9 ± 0.5	0.155 ± 0.017	2.48 ± 0.33	600 ± 50	200 ± 30
SiO(2–1)[e]	0.92 ± 0.14	0.26 ± 0.04	0.72 ± 0.13	800 ± 100	539 ± 11
SiO(2–1)[f]	0.70 ± 0.17	0.20 ± 0.06	0.72 ± 0.13	500 ± 50	...
$H^{13}CO^+(3–2)$[f]	1.63 ± 0.25	0.052 ± 0.008	1.15 ± 0.24	300 ± 50	110 ± 40
$H^{13}CO^+(1–0)$[f]	0.22 ± 0.06	0.062 ± 0.018	0.16 ± 0.11	450 ± 50	220 ± 190
$HN^{13}C(3–2)$	8.4 ± 1.0	0.26 ± 0.03	2.22 ± 0.31	700 ± 50	408 ± 10

Notes.
[a] Fluxes are estimated from the Gaussian fitting components in Figures 2–5, which are listed in Appendix B in Table 8. Uncertainties in the fluxes and L' are estimated from the fitting covariance matrices and the absolute flux calibration (10%). While the total flux in the $HC^{15}N(3–2)+SO(6_6–5_5)$ line blend is relatively well constrained, the contribution of each species is extremely uncertain, indicated by their >200% uncertainties.
[b] For consistency with HCN single dish data used in the analysis we include source integrated L' values: $L' = 3.25 \times 10^7(\nu_{obs}/\mathrm{GHz})^{-2}(D_L/\mathrm{Mpc})^2(1+z)^{-3}(\int_{\Delta v} S_v dv/\mathrm{Jy\,km\,s^{-1}})$, (Solomon et al. 1992)
[c] Peak of the line profile extracted from single spaxels toward the continuum centers. Relative errors on 1.2 mm data are ±0.21 K, on the 3.5 mm data are ±0.11 K, but in almost all cases these are insignificant compared to the absolute 10% calibration uncertainty.
[d] Where multiple Gaussian components are required to fit the line, we use a non-parametric FWHM derived from the intensity weighted mean width inspired by Bothwell et al. (2013), in the discreet form as: $\mathrm{FWHM_{iwm}} = 2\sqrt{2\ln 2}(\sum_i (v-\bar{v})^2 |I_i|\Delta v/\sum_i |I_i|\Delta v)^{0.5}$. Note that this method is very sensitive to both the location of the line center (and hence to the assumed redshift) and to noise at the ends of the fainter lines: this method becomes increasingly susceptible to noise at low S/N.
[e] Case 1: no $H^{13}CO^+$.
[f] Case 2: with $H^{13}CO^+$.

isotopologue lines respectively. For a T_B ratio of 8 we find $\tau_{12} \geqslant 7$. This is almost 20 times higher than the optical depth measured in absorption in the WN by Sa09. If we instead use the optical depth for the WN from Sa09 (0.36), we find a predicted $H^{13}CO^+(3–2)$ $T_B \sim 0.27$ K, approximately at the 1σ noise level. In this case, the $H^{13}CO^+(3–2)$ WN line would be completely blended with SiO(6–5), its contribution wholly undetectable, and the SiO(6–5) would extend redward to +500 km s^{-1}, almost far as $HCO^+(3–2)$. We interpret this as weak evidence for an insignificant $H^{13}CO^+(3–2)$ contribution in the WN.

In the EN, Sa09 observed a much higher optical depth in absorption $\tau_{12} = 3.7$. This predicts an $H^{13}CO^+(3–2)$ $T_B \sim 1.0$ K, exactly as is observed in our data.

While these estimates are extremely uncertain, including multiple simplifying assumptions, they do offer the tantalizing possibility that while the $H^{13}CO^+(3–2)$ line in the EN is real, and accurately determined, the line that is suspected to be $H^{13}CO^+(3–2)$ in the WN is almost entirely SiO(6–5), with $H^{13}CO^+(3–2)$ contributing at the same level as random noise.

The evidence from the above kinematic, spatial and line brightness analyses casts doubt on the identification of $H^{13}CO^+(3–2)$ in the WN, but we do not believe that it is sufficient to rule it out entirely. It seems much more likely that $H^{13}CO^+(3–2)$ has been observed in the EN, but this conclusion rests upon numerous assumptions. As we cannot rule clearly for one side or another, in either nucleus, we therefore proceed working with two limiting cases which can apply to each nucleus independently.

1. Case 1: we have no detection of $H^{13}CO^+$ in either the (1–0) or (3–2) transition.
2. Case 2: the fitted components near the $H^{13}CO^+(1–0)$ and (3–2) line centers are purely $H^{13}CO^+$, with no contamination (other than that from the other fitted components).

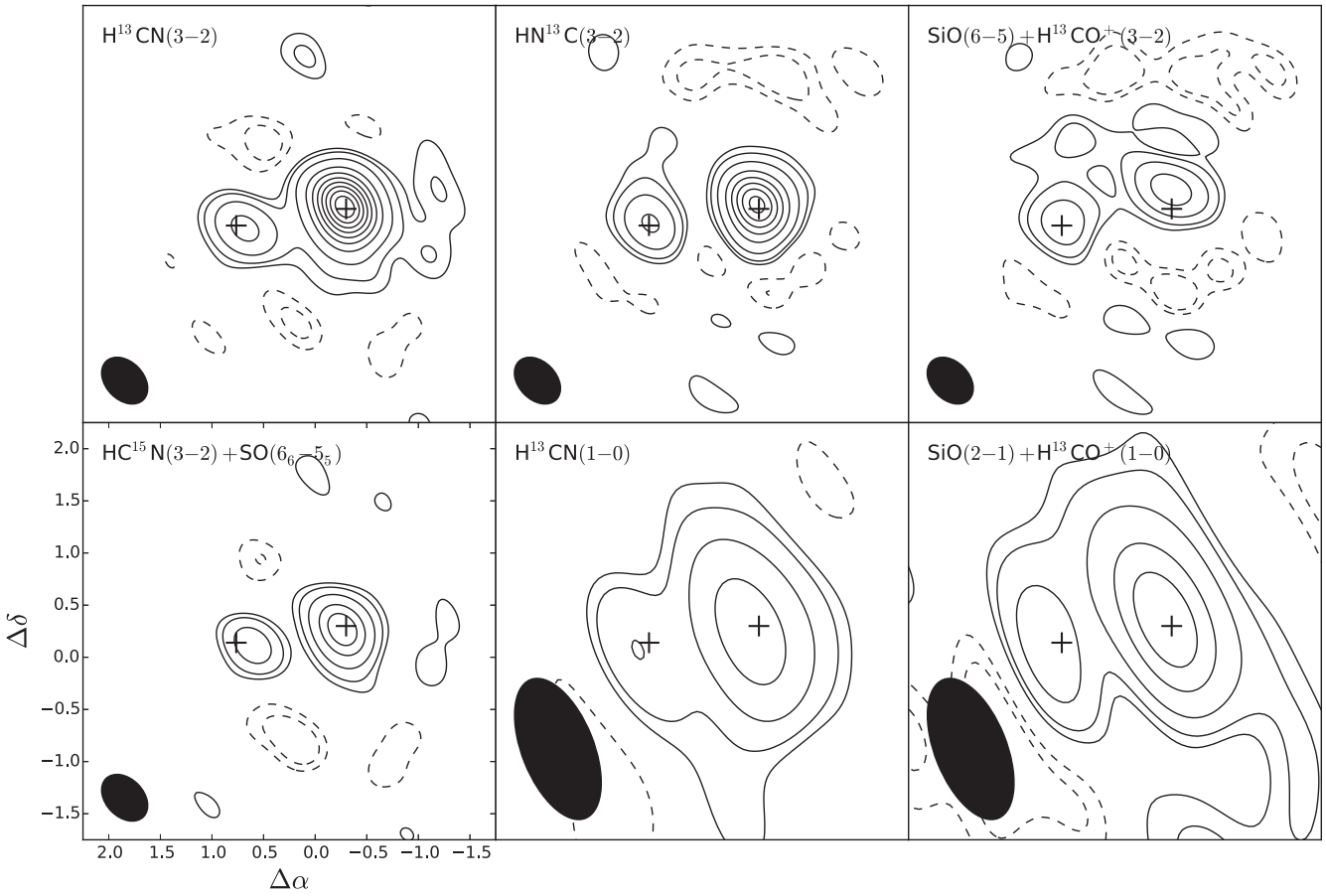

Figure 7. Line integrated contour plots of the observed species. Contours are at -5, -3, 3, 5, and $10n\sigma$, for $n = 1, 2...10$. The synthesized beams are $0\farcs52 \times 0\farcs37$ and $1\farcs44 \times 0\farcs70$ and are shown in the bottom left corners of the plots. Crosses mark the continuum centers. The 5σ sidelobe contours suggest that our observations are dynamic range limited.

4. WESTERN NUCLEUS

The WN line profiles all share similar features, although there is a significant variation between the 3.5 mm and 1.2 mm spectra. The 1.2 mm lines show a distinct asymmetry, peaking just redward of the line center but with the majority of the velocity integrated emission blueward of the line. Of particular interest are $H^{13}CN$ and SiO, which are not only the brightest lines, but those with the most complex line profiles.

The SiO(6–5) line is especially complex, both spectrally (requiring 5 Gaussian components including the possible $H^{13}CO^+$(3–2) component), and spatially, with multiple components in the WN. The intriguing spatial distribution seen in Figure 7 is explored in Figure 8 where we present the SiO(6–5) channel maps. The overall peak emission and absorption are $\sim 0\farcs1$ north and south of the continuum center and in the $+115\,\mathrm{km\,s^{-1}}$ and $-115\,\mathrm{km\,s^{-1}}$ channels respectively, while the full SiO(6–5) data cube has 1σ continuum absorption extending as far north as the peak of the SiO(6–5) emission. The peak emission and absorption in the $0\,\mathrm{km\,s^{-1}}$ channel map only has an even greater separation, almost $0\farcs4$, clearly indicating that the offset is real, and not due to radio seeing effects. The northwestern offset of the SiO(6–5) emission peak from the continuum center was also seen in CO(2–1) observations by Downes & Eckart (2007). Fractional absorption against the continuum implies a lower limit for the optical depth, $\tau_{\mathrm{SiO(6-5)}} \geqslant 0.25$ toward the absorption peak.

In Figure 9 we show position-velocity slices across the two nuclei. Slices are $1\farcs2$ long, centered on the continuum centers and taken at 270° across the WN (east to west) and 225° across the EN (southeast to northwest) to be consistent with Sa09. The velocity slices have been smoothed with a Gaussian kernel for clarity. While the EN signal is too weak to identify any clear trends, the WN $H^{13}CN$(3–2) and SO(6_6–5_5) lines both display evidence of disk-like rotation. The SiO(6–5) line shows signs of a strong, kinematically extended outflow with the P Cygni like absorption at negative velocities mixed with an emission signature at $\sim -300\,\mathrm{km\,s^{-1}}$, coincident with the peak blueshifted emission in the $H^{13}CN$(3–2) line. There is a clear systemic velocity offset between the two nuclei, as reported in the literature, potentially as large as $90\,\mathrm{km\,s^{-1}}$ based on our data, but the asymmetry and width of the lines makes reliably identifying the precise value of the offset highly uncertain. We therefore adopt the $60\,\mathrm{km\,s^{-1}}$ CO derived offset of Sa09, which is reliably determined from narrow, on line center, absorption in the CO lines.

Figure 9 reveals the blueward absorption extending all the way out to $-600\,\mathrm{km\,s^{-1}}$, with no equivalent redshifted emission, even in the case 1 limit. However, if we temporarily exclude the blueshifted emission peak at $-300\,\mathrm{km\,s^{-1}}$ the emission and absorption appear symmetric about a point $\sim -50\,\mathrm{km\,s^{-1}}$. This profile is suggestive of a symmetric outflow, traced by SiO, merged with SiO emission from the nuclear disk itself.

In case 2 the reddest peak in the SiO(6–5) line profile is attributed entirely to $H^{13}CO^+$(3–2). This case seems unlikely

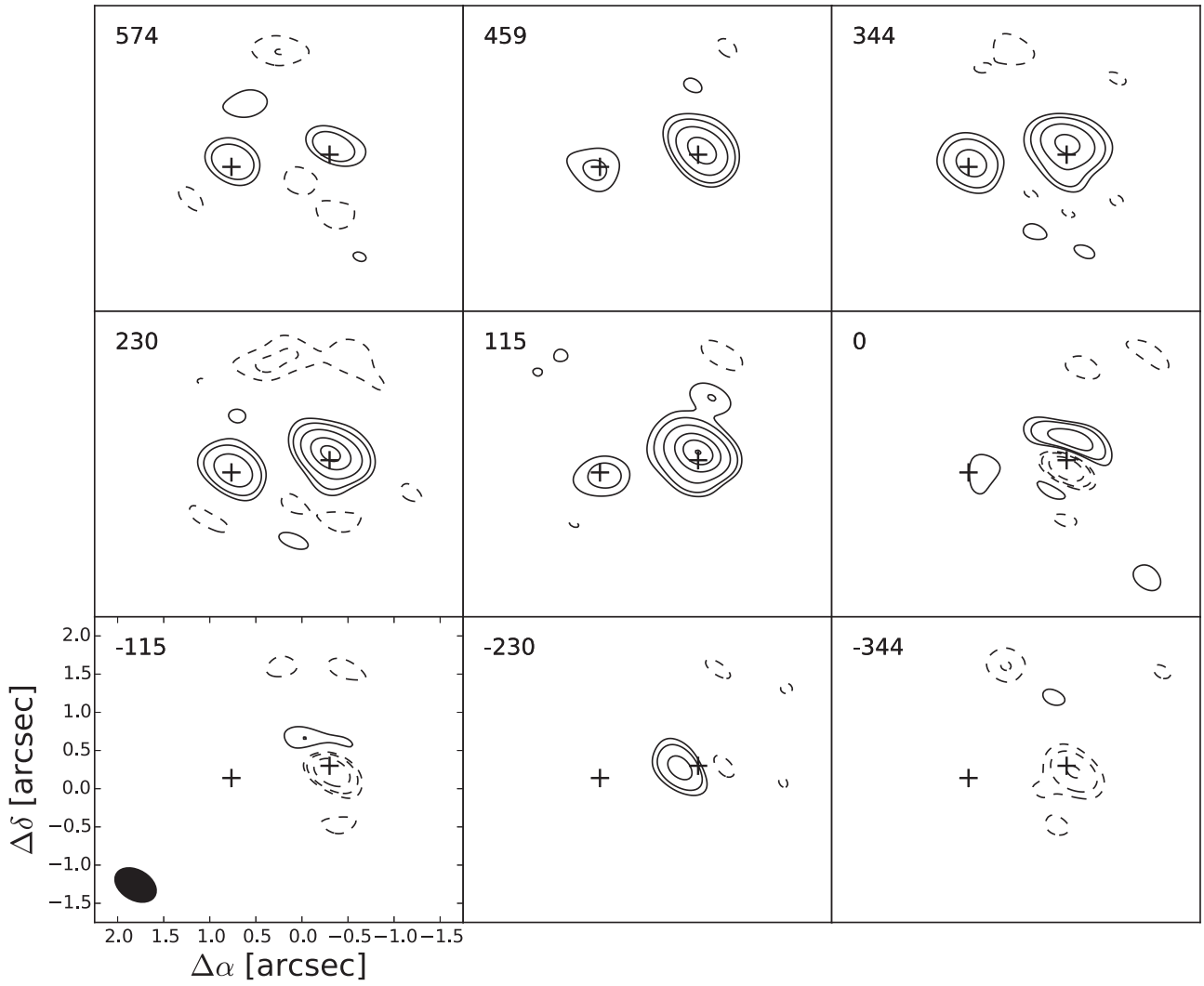

Figure 8. Channel maps for the SiO(6–5) line complex, including the subsidiary emission (at $-230\,\mathrm{km\,s^{-1}}$) and absorption (at $-344\,\mathrm{km\,s^{-1}}$). Channels have been averaged to $115\,\mathrm{km\,s^{-1}}$. Contours are at -10, -5, -3, 3, 5, and $10n\sigma$ intervals ($1\sigma = 0.63$ mJy beam^{-1}). The mean velocity of each channel relative to the line center is given in the top left corners of the plots. Note the eastward offset of the emission at $-230\,\mathrm{km\,s^{-1}}$ and the colocation of the sub-continuum absorption red and blueward of this subsidiary peak ($-115\,\mathrm{km\,s^{-1}}$ and $-344\,\mathrm{km\,s^{-1}}$). The $0\farcs52 \times 0\farcs37$ synthesized beam is shown in the bottom left panel. The crosses mark the continuum centers.

as the emission at these velocities is concentrated north of the continuum (Figure 8), whereas the HCO^+(3–2) emission of Sa09 is continuum centered and spatially very similar to our $H^{13}CN$(3–2) line (Figure 7). It is clear from Figure 9 that case 1 implies that SiO reaches higher velocities than $H^{13}CN$, but it is still not as extended in velocity as HCO^+ (Figure 6), which extends almost $200\,\mathrm{km\,s^{-1}}$ further redward in emission.

It is worth noting that while SiO(6–5) shows significant absorption in the WN, SiO(2–1) has no sign of continuum absorption. As was noted in Sa09, the high brightness temperature of the dust in the WN implies that higher frequency transitions are more likely to be seen in absorption against the dust continuum, and indeed in the far-IR almost all molecular lines are observed in absorption (González-Alfonso et al. 2004; González-Alfonso et al. 2012), so the lack of absorption in the SiO(2–1) line could simply be due to the drop in dust SED between 1.2 mm and 3.5 mm. Sa09 further noted that the Einstein coefficients for photo-absorption could be having an effect. Assuming detailed balance:

$$\mathrm{B}_{lu} = \frac{g_u}{g_l}\mathrm{A}_{ul}\left(\frac{2\mathrm{h}\nu^3}{c^2}\right)^{-1}, \qquad (3)$$

which for the rotational transitions of linear diatomic molecules may be written as:

$$\mathrm{B}_{J,J+1} = \frac{2J+3}{2J+1}\mathrm{A}_{J+1,J}\left(\frac{2\mathrm{h}\nu^3}{c^2}\right)^{-1}, \qquad (4)$$

gives for SiO $\mathrm{B}_{56}/\mathrm{B}_{12} \simeq 1$, with similar results in other lines (since $\mathrm{A}_{ul} \propto \nu^3$): this effect is most significant when comparing similar frequency transitions of different molecules. This suggests that the absence of absorption in our SiO(2–1) lines is more likely a dust brightness effect. It does not appear to be a beam size issue: the absorption is still clearly visible when the SiO(6–5) cube is smoothed to the 3.5 mm beam size. Finally, we consider the possibility that there is an angularly extended "screen" of blueshifted emission in front of the WN which is being spatially filtered in the 1.2 mm observations. The minimum baselines were 22.6 kλ and 36.4 kλ at 1.2 mm and 3.5 mm respectively, so nominally we resolve out emission on angular scales greater than 9.″1 and 5.″7. Therefore the baselines are not likely to be responsible for the absence of absorption: the 3.5 mm observations will resolve out emission before the 1.2 mm, whereas the line profiles could only be explained if the

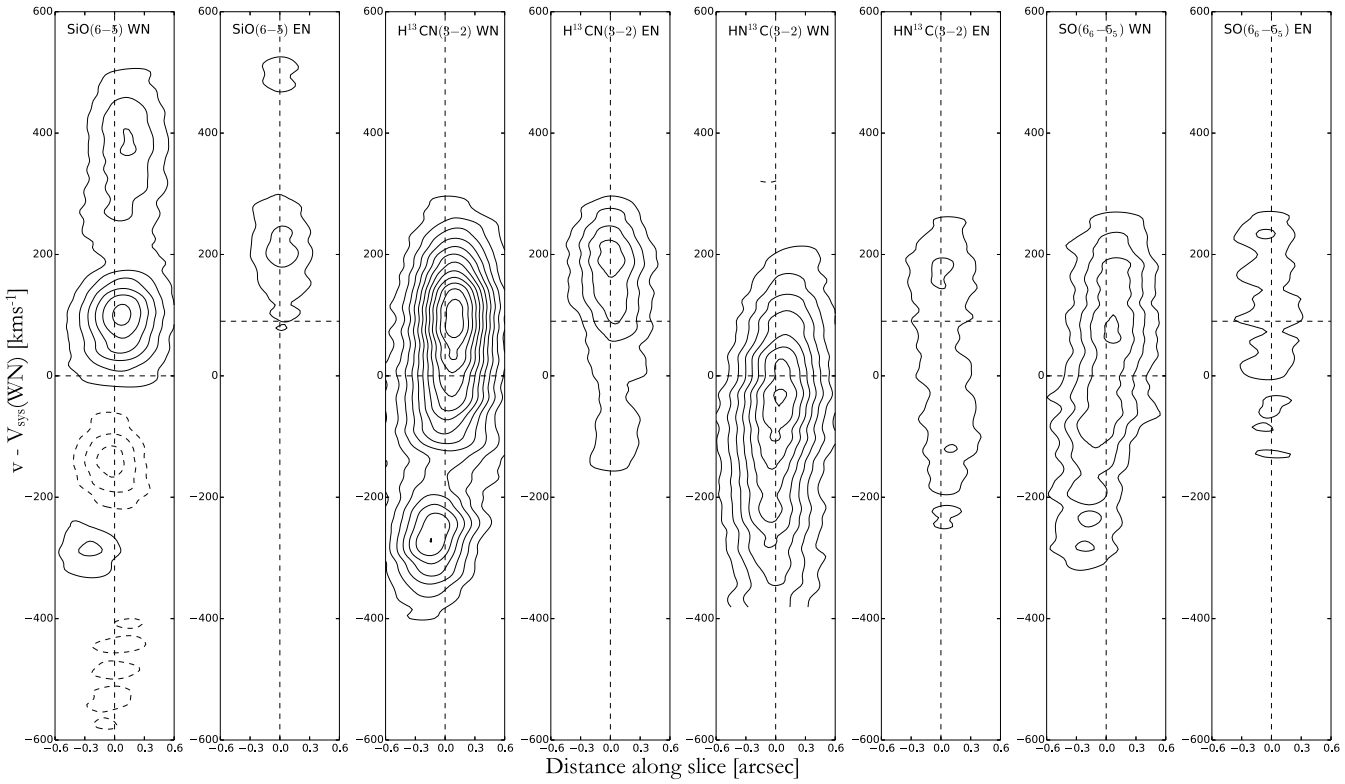

Figure 9. Velocity slices across the two nuclei of Arp 220. Slices are centered on the systemic velocity (radio, LSR) of the WN, 5355 km s^{-1}, to highlight the offsets between the two nuclei. Slices are 1.″2 long, centered on the continuum centers and taken at 270° across the WN (east to west) and 225° across the EN (southeast to northwest) to be consistent with Sa09. The horizontal axis corresponds to the angular distance along the slice. Contours are at $\pm 3n\sigma$. The H^{13}CN and SO WN slices suggest disk like rotation. The SiO WN slice could be indicative of rotation, an outflow or a combination of the two. Its prominent P Cygni profile is clearly seen, but the emission peaks at $\sim$100 km s^{-1} and ~ -300 km s^{-1} and absorption trough at ~ -150 km s^{-1} are almost precisely coincident with the two peaks and the minimum in the H^{13}CN WN slice, suggesting they are tracing, at least in part, the same kinematics.

1.2 mm observations were resolving out large-scale, blueshifted emission.

The H^{13}CN(3–2) line is the brightest line observed at 1.2 mm. We would expect this line to trace the same high density star forming environment traced by HCN(1–0), (3–2) and (4–3) as observed by Greve et al. (2009) and we find the emission strongly correlated with the continuum emission (Figure 7). The H^{13}CN slice (Figure 9) suggests predominantly disk like rotation, although our spatial resolution is insufficient for successful kinematic modeling. However, comparison with the SiO WN slice with emission peaks at $\sim$100 km s^{-1} and ~ -300 km s^{-1} and the absorption trough at ~ -150 km s^{-1} shows that they are almost precisely coincident with the two peaks and the minimum in the H^{13}CN WN slice suggesting they are tracing, at least in part, the same gas. However, if they are tracing the same gas, it is curious that they have such different levels of absorption. The simplest explanation is that while H^{13}CN(3–2) is tracing both the dense, star forming nuclear disk and an outflow, presenting as a P Cygni profile embedded within a Gaussian line, while SiO(6–5) traces the outflow with only a small component in the star forming nuclear disk.

We also examine the possibility that H^{13}CN(3–2) and SiO(6–5) are tracing similar regions, but that the different line profiles are driven by the different properties of the transitions. The H^{13}CN $J = 3$ and SiO $J = 6$ levels have energies of 24.9 K and 43.8 K respectively (Remijan et al. 2007; Müller et al. 2005). Coupled with the fact that higher J transitions are harder to excite, as they need the intermediate J levels to be excited as well, the P Cygni profile in H^{13}CN(3–2) could be less prominent because the H^{13}CN $J = 3$ level is easier to excite, so is seen more in emission, while SiO(6–5) is seen in absorption. However, the HCO$^+$ $J = 3$ level has an energy of 25.7 K (Remijan et al. 2007), only 3% higher than that of H^{13}CN $J = 3$, and is seen with strong absorption (Sa09), suggesting that the energies alone cannot fully explain the differences in the line profiles. Furthermore, it does not appear to be a critical density effect, since the critical densities for H^{13}CN(3–2), SiO(6–5) and HCO$^+$(3–2) are 2.9×10^6 cm^{-3}, 2.0×10^6 cm^{-3} and 7.8×10^5 cm^{-3} respectively. It would appear therefore to be either an optical depth effect, or that the majority of the H^{13}CN(3–2) emission is tracing the nuclear disks, with a small component in the outflow traced by SiO(6–5). This would imply however that there should be the same $\pm$40 pc emission and absorption offset seen in SiO(6–5) in the H^{13}CN(3–2) line, which would shift the integrated contour peak north (as can be seen for SiO(6–5) in Figure 7); this is not seen, but could simply be a sign that H^{13}CN in the outflow is too faint to significantly affect the integrated plots.

HN^{13}C(3–2) emission extends beyond the end of our spectrum, making it impossible to reliably compare it with the H^{13}CN(3–2) emission. The absorption present in H^{13}CN(3–2) appears to be absent in HN^{13}C(3–2). This could be due to errors at the edges of the bandpass, or it could be the same effect as has been seen in single dish spectra, where HCN(3–2) shows absorption but HNC(3–2) does not, possibly due to mid-IR pumping or maser emission in HNC (Aalto et al. 2009). Alternatively, it could be a sign of HCN enhancement (over HNC) in the shocks in the outflow (e.g., Mitchell 1984; Bachiller & Pérez Gutiérrez 1997; Martín et al. 2014). This would be consistent with the case above, where H^{13}CN is over abundant in an outflow from the center of the nucleus as well as being prevalent throughout the

nuclear disk. Both isomers trace the circumnuclear disk (CND), but only $H^{13}CN$ would be detectable in the outflow, imprinting a P Cygni profile on to the $H^{13}CN$ line profile but not the $HN^{13}C$.

Like SiO, SO in the Milky Way is a shock tracer (Chernin et al. 1994), ubiquitous in star forming regions. It is unclear whether these remain reliable shock tracers extragalactically, where excitation and abundance effects could be more significant. Given the uncertainty in the fitting for $SO(6_6–5_5)$ and $HC^{15}N(3–2)$ we cannot reliably separate the two lines and they are not focused on in this work. Similarly, we see a trace of the $SO(2_2–1_1)$ line at the red end of the 3.5 mm WN spectrum, but this is severely affected by edge effects in the bandpass and is not included in the analysis.

5. EASTERN NUCLEUS

While none of the lines in the EN are spatially resolved, SiO(2–1), SiO(6–5), $HN^{13}C(3–2)$ and $H^{13}CN(3–2)$ all show doubly peaked emission with no significant sign of sub-continuum absorption (while in case 1 the SiO(2–1) and (6–5) spectra both show possible signs of the same absorption-emission-absorption structure seen in the WN, this is not spatially correlated across the channels and is below 1σ).

The SiO line profiles in the EN are very similar: the (6–5) line has major and minor peaks at V_{sys} + 140 km s^{-1} and V_{sys}–175 km s^{-1} respectively, cf. V_{sys} + 150 km s^{-1} and V_{sys}–200 km s^{-1} in the (2–1) line. We do not see the prominent P Cygni profiles observed in the HCO^+(3–2) and (4–3) lines in the EN (Sa09), although the 3.5 mm spectrum in particular does allow for some degree of blueward absorption around −100 km s^{-1}. Only the absolute scaling of the line profile changes across the EN. This may explain the lack of a clear P Cygni profile in the EN, since the resolution of Sa09 was almost double ours, we may be smearing out any sub-continuum absorption in the EN. If the $\sim 1\sigma$ signs of continuum absorption in the EN are real, then this implies $\tau_{SiO(6–5)} \simeq 0.03 \pm 0.01$: 1/10 the WN value.

6. ANALYSIS

6.1. LVG Modeling

The large velocity gradient (LVG) code RADEX[8] was used with line ratios, derived from our earlier analysis and presented in Table 3, to provide estimates of the molecular hydrogen density (n_{H_2}), molecular column density over velocity width ($N_x/\Delta v$) and kinetic temperature (T_k) for our observed species. The column densities provide abundance ratios $[H^{13}CN]/[SiO]$ and $[H^{13}CN]/[H^{13}CO^+]$. These simple models do not account for the potentially significant mid-IR pumping in Arp 220. Since our beam is averaging over ∼200 pc × 140 pc, we are certainly including a wide range of regions including giant molecular clouds (GMCs), hot cores, shocked regions, photon dominated regions (PDRs) and perhaps an XDR if there is an AGN at the center of the WN, so the model parameters are at best only representative of the conditions of the dominant emission regions.

We first used HCN and $H^{13}CN$ data from Greve et al. (2009; which includes data from Solomon et al. 1992 and Krips et al. 2008) and from our work to find the best fitting parameters for Arp 220 as a whole, then used these to model abundance ratios for SiO and $H^{13}CO^+$ in the two nuclei independently.

[8] A non-LTE code for radiative transfer, available here: http://home.strw.leidenuniv.nl/~moldata/radex.html.

Table 3
Line Brightness Temperature Ratios for the Two Nuclei

L' Ratios	
Line Ratio	Ratio
$L'(HCN(3–2))/L'(HCN(1–0))$	0.79 ± 0.12
$L'(H^{13}CN(3–2))/L'(H^{13}CN(1–0))$	1.60 ± 0.24
$L'(HCN(3–2))/L'(H^{13}CN(3–2))$	5.0 ± 0.8
$L'(HCN(1–0))/L'(H^{13}CN(1–0))$	10.1 ± 1.3

$T_B dv$ Line Integrated Ratios[a]		
Line Ratio	WN	EN
$H^{13}CN(3–2)/H^{13}CN(1–0)$	6.7 ± 0.9	5.8 ± 0.9
$H^{13}CN(3–2)/HN^{13}C(3–2)$	1.41 ± 0.07	1.51 ± 0.10
Case 1[b]: no $H^{13}CO^+$		
$H^{13}CN(3–2)/SiO(6–5)$	2.32 ± 0.12	2.0 ± 0.3
$H^{13}CN(1–0)/SiO(2–1)$	0.826 ± 0.016	0.54 ± 0.07
$H^{13}CN(3–2)/H^{13}CO^+(3–2)$	>41	>10
$H^{13}CN(1–0)/H^{13}CO^+(1–0)$	>9	>3
$SiO(6–5)/SiO(2–1)$	2.4 ± 0.3	1.61 ± 0.22
Case 2: $H^{13}CO^+$		
$H^{13}CN(3–2)/SiO(6–5)$	4.0 ± 0.5	2.60 ± 0.11
$H^{13}CN(1–0)/SiO(2–1)$	0.890 ± 0.027	0.71 ± 0.16
$H^{13}CN(3–2)/H^{13}CO^+(3–2)$	4.78 ± 0.23	7.8 ± 0.9
$H^{13}CN(1–0)/H^{13}CO^+(1–0)$	11.5 ± 2.3	2.3 ± 0.6
$SiO(6–5)/SiO(2–1)$	1.47 ± 0.23	1.6 ± 0.4

$T_{B,peak}$ Ratios[c]		
Line Ratio	WN	EN
$H^{13}CN(3–2)/H^{13}CN(1–0)$	5.8 ± 0.9	8.6 ± 2.1
$SiO(6–5)/SiO(2–1)$	3.4 ± 0.6	2.8 ± 0.7
$H^{13}CN(3–2)/H^{13}CO^+(3–2)$	4.1 ± 0.3	1.72 ± 0.13
$H^{13}CN(1–0)/H^{13}CO^+(1–0)$	9 ± 5	5 ± 3
$H^{13}CN(3–2)/SiO(6–5)$	1.95 ± 0.08	1.98 ± 0.03
$H^{13}CN(1–0)/SiO(2–1)$	1.19 ± 0.11	0.79 ± 0.05
$HN^{13}C(3–2)/H^{13}CN(3–2)$	0.689 ± 0.023	0.453 ± 0.010

Notes.
[a] Based on the fitted Gaussian components, using only the emission components. The $H^{13}CN(3–2)/(1–0)$ and $SiO(6–5)/(2–1)$ ratios are quoted here without corrections for beam dilution.
[b] Upper limits on $H^{13}CO^+$ contribution estimated 1σ Gaussians with FWHM of 200 km s^{-1}.
[c] Peak of the line profile extracted from single spaniels toward the continuum centers in the unsmoothed maps: these ratios do not account for beam dilution in ratios of 1.2 mm and 3.5 mm lines.

6.1.1. HCN

We recalculated the L' values of HCN 3–2 and 1–0 as weighted averages of the data reported in Greve et al. (2009) using their quoted $S_\nu\,dv$ values and our adopted cosmological parameters, finding $L'_{HCN(3–2)} = 9.5 \pm 1.1 \times 10^8$ K km s^{-1} pc^2 and $L'_{HCN(1–0)} = 12.1 \pm 1.2 \times 10^8$ K km s^{-1} pc^2.

The background temperature (T_{bg}) was set to 45 K and 110 K (Mangum et al. 2013 and GA12 respectively), and we modeled the kinetic gas temperature (T_k) as 70, 100, 150, 300, 350 and 450 K. The molecular hydrogen density (n_{H_2}) was varied from 10^4–10^8 cm^{-3} in $\log_{10}$ steps of 0.02, and N_{HCN} was varied from 6×10^{14}–6×10^{17} cm^{-2} in $\log_{10}$ steps of 0.015. We assume throughout that $\Delta v = 100$ km s^{-1}. We further assumed $[HCN]/[H^{13}CN] = 60$ (e.g., Langer & Penzias 1993), and found χ^2 values for the results grids which are shown in Figure 10.

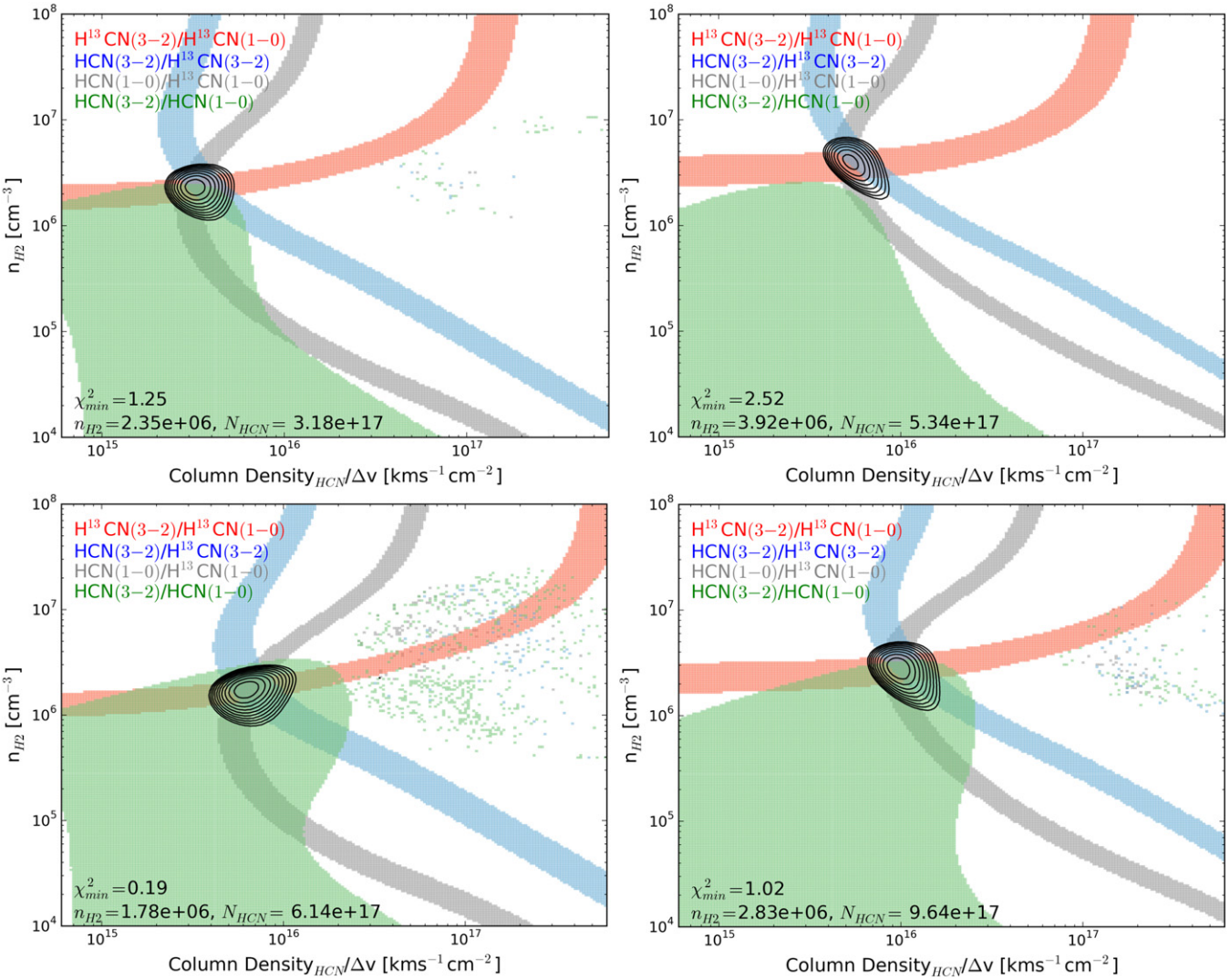

Figure 10. Best fitting parameters for the HCN and $H^{13}CN$ ratios. Top: $T_k = 150$ K, bottom $T_k = 300$ K, left $T_{bg} = 45$ K, right $T_{bg} = 110$ K. The 1σ regions of individual ratios are highlighted, and the χ^2 contours from 1 to 10 in steps of 1 are shown. The "dotting" in the upper right corner is due to localized non-convergences in the LVG code, and does not affect our results at these temperatures. These results imply $T_k \geqslant 150$ K and prefer $T_{bg} = 45$ K for all T_k, and as such we identify the $T_k = 150$ K, $T_{bg} = 45$ K as the best fit ($\chi^2_{min} = 1.25$. The best fit parameters are found from weighted averages of four best fits shown above, and we find $n_{H_2} = 2.1 \pm 0.6 \times 10^6$ cm^{-3} and $N_{HCN}/\Delta v = 6.2 \pm 1.6 \times 10^{15}$ cm^{-2} km^{-1} s.

For both T_{bg} values, the models exclude low kinetic temperatures ($T_k \lesssim 100$ K), which can fit the $H^{13}CN(3–2)/(1–0)$ ratios alone but not the very optically thick HCN. For any given T_k the models prefer the lower $T_{bg} = 45$ K. We find reduced $\chi^2 = 1.25$ at $T_k = 150$ K and $T_{bg} = 45$ K and this continues to decrease as T_k increases toward 500 K. Above this temperature we have no HCN transition data and our RADEX solutions begin to diverge rapidly. We adopt $T_k = 150$ K and $T_{bg} = 45$ K as our best fit solution, being wary of over-fitting, but note that the higher T_k is consistent with the NH_3 thermometry of Mangum et al. (2013). The green band in Figure 10, showing the parameters fitting the observed ratio to within 1σ for the $L'(HCN(3–2))/L'(HCN(1–0))$ line ratio, is much wider than for the other lines. This ratio of two optically thick lines is only weakly dependent upon n_{H_2} and $N_{HCN}/\Delta v$ (provided $N_{HCN}/\Delta v$ is high enough for the line to be optically thick), and varies slowly across the explored parameter space. The four solutions shown in Figure 10 are our four best fits below 350 K. Given the lack of a clearly superior fit, we find the best fit n_{H_2} and $N_{HCN}/\Delta v$ from χ^2_ν weighted averages. We find $n_{H_2} = 2.1 \pm 0.6 \times 10^6$ cm^{-3} and $N_{HCN}/\Delta v = 6.2 \pm 1.6 \times 10^{15}$ cm^{-2} km^{-1} s.

Since the χ^2 values for the HCN−$H^{13}CN$ LVG models continue to decrease at higher temperatures, we also consider the case that the HCN and $H^{13}CN$ emission is dominated by shocks. We repeated the following $H^{13}CN$, $H^{13}CO^+$ and SiO analysis with $T_k = 450$ K and $T_{bg} = 110$ K, and find that while the column densities found are a dex higher for all species, the abundance ratios are only slightly changed and are consistent within uncertainties. The abundance ratios presented below are robustly determined, even if the kinetic temperature and background temperatures are not.

Our best fit T_k and n_{H_2} are consistent with the maximum likelihood parameters of Rangwala et al. (2011), which are based on both low J HCN emission and high J absorption seen with Herschel, while our N_{HCN} is two orders of magnitude higher. They found $T_k = 320$ K, $n_{H_2} = 2 \times 10^6$ cm^{-3} and $N_{HCN} = 2 \times 10^{15}$ cm^{-2}. GA12 found, for $T_{bg} = 110$ K, $T_k \sim 150$ K, $n_{H_2} = 4–8 \times 10^5$ cm^{-3} and $N_{HCN} = 6–4 \times 10^{17}$ cm^{-2}.

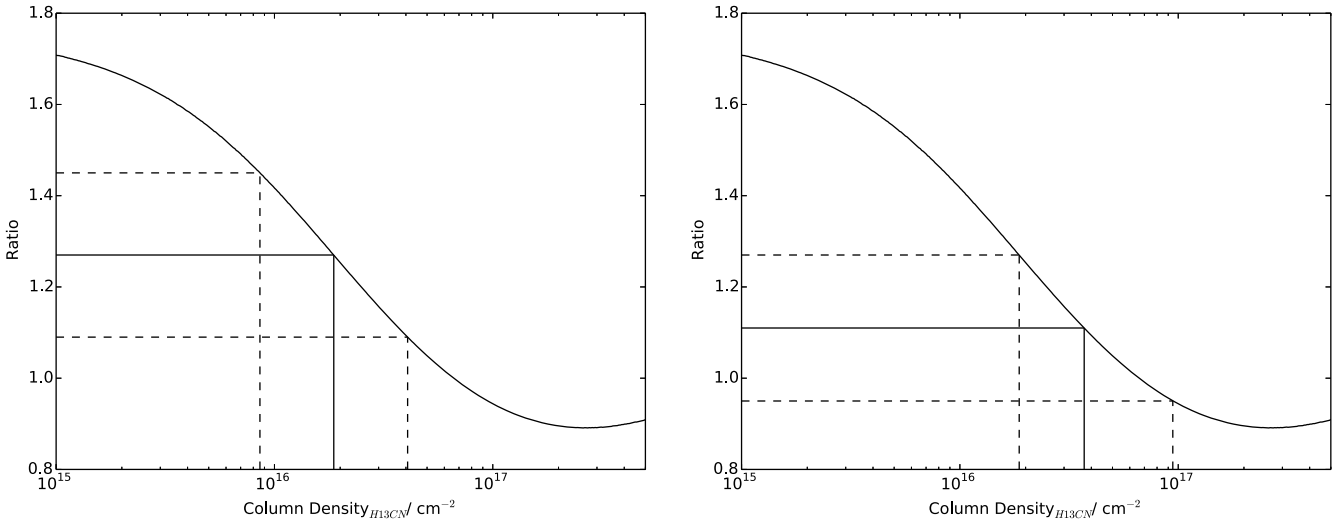

Figure 11. $H^{13}CN$ column densities found in the WN and EN (left and right respectively). The dashed lines indicate the error bounds. We find column densities $N_{H^{13}CN}/\Delta v = 1.9^{+2.2}_{-1.0} \times 10^{14}$ cm^{-2} km^{-1} s and $N_{H^{13}CN}/\Delta v = 3.7^{+5.7}_{-1.8} \times 10^{14}$ cm^{-2} km^{-1} s in the WN and EN respectively.

While our analysis prefers $T_{bg} = 45$ K, for the T_{bg} and T_k of GA12 we find $n_{H_2} = 3.6 \pm 1.5 \times 10^6$ cm^{-3} and $N_{HCN} = 6 \pm 3 \times 10^{17}$ cm^{-2}. Our best fitting model with $T_{bg} = 45$ K and $T_k = 150$ K gives $n_{H_2} = 2.1 \pm 0.6 \times 10^6$ cm^{-3} and $N_{HCN}/\Delta v = 6.2 \pm 1.6 \times 10^{15}$ cm^{-2} km^{-1} s, consistent with GA12. There is some tension with earlier millimetre studies of HCN in Arp 220, which found best fitting parameters of $45\,\mathrm{K} < T_k < 120\,\mathrm{K}$ and $n_{H_2} = 0.3 \times 10^6$ cm^{-3} (Greve et al. 2009). We note that while Rangwala et al. (2011); Greve et al. (2009) and this work all use simple LVG codes, GA12 used a more complex, multiphase model including dust attenuation. All of the above used HCN data averaged over the two nuclei, and only GA12 includes mid-IR pumping. Their results suggested that mid-IR pumping is not having a significant effect on the vibrational ground state, high-J HCN population, but the effect on the low-J transitions may be more significant.

Having found the "average" parameters for the HCN and $H^{13}CN$ in Arp 220, we use the high resolution of our observations to test for chemical differences between the nuclei. To this end, we ran RADEX again, fixing all parameters to the best fit HCN solution except for the $H^{13}CN$ column density, and fitted this to the beam dilution corrected $T_B dv$ ratios for $H^{13}CN$ (3–2)/(1–0), 1.27 ± 0.18 and 1.11 ± 0.16 in the WN and EN respectively. The results are shown in Figure 11. We find $N_{H^{13}CN}/\Delta v = 1.9^{+2.2}_{-1.0} \times 10^{14}$ cm^{-2} km^{-1} s in the WN and $N_{H^{13}CN}/\Delta v = 3.7^{+5.7}_{-1.8} \times 10^{14}$ cm^{-2} km^{-1} s in the EN. We note that these solutions are optically thick, with optical depths from 1 to 6.

6.1.2. $H^{13}CO^+$

For $H^{13}CO^+$ we analyze the two nuclei separately, making use of the $T_B dv$ ratios of $H^{13}CN(3–2)/H^{13}CO^+(3–2)$ and $H^{13}CN(1–0)/H^{13}CO^+(1–0)$, which do not require corrections for beam dilution (see Table 3). We use a simple two phase model, where the $H^{13}CN$ column and n_{H_2} are fixed to the values found above for the WN and EN (with $\Delta v = 100$ km s^{-1}). In case 1 we fix n_{H_2} for $H^{13}CO^+$, as with only upper limits we cannot simultaneously constrain the hydrogen density and column density, while in case 2 n_{H_2} and $N_{H^{13}CO^+}/\Delta v$ for $H^{13}CO^+$ are allowed to vary over the full range described previously for the $HCN/H^{13}CN$ modeling. In both cases T_k and T_{bg} are fixed to the best fit values of 150 K and 45 K respectively from the previous section. We perform the analysis for both case 1 and case 2. We ran grids using the upper, middle and lower values for the $H^{13}CN$ column density found above, and used the maximum and minimum values of the resultant $H^{13}CO^+$ column density to estimate uncertainties.

Case 1: the column densities permitted by the lower limit ratios are shown in Figure 12. We find upper limits on the $H^{13}CO^+$ column density of 2×10^{11} cm^{-2} km^{-1} s and 2×10^{12} cm^{-2} km^{-1} s in the WN and EN respectively. These correspond to lower limits on the abundance ratio $[H^{13}CN]/[H^{13}CO^+]$ of 1000 and 200 in the WN and EN respectively. These extremely high limits are dramatically decreased by reducing n_{H_2} in the $H^{13}CO^+$ phase, and at $n_{H_2} = 5 \times 10^4$ cm^{-3} the limits are 44 and 60.

Case 2: we found best fit solutions in the two nuclei $N_{H^{13}CO^+}/\Delta v = 8^{+7}_{-4} \times 10^{12}$cm^{-2} km^{-1} s in the WN and $N_{H^{13}CO^+}/\Delta v = 1.9^{+6.6}_{-1.3} \times 10^{14}$cm^{-2} km^{-1} s in the EN. The grids for the best fit $H^{13}CN$ column densities are shown in Figure 13. The uncertainties are predominantly driven by the uncertainty in the $H^{13}CN$ column density, so that the abundance ratio $[H^{13}CN]/[H^{13}CO^+]$ is relatively well determined as 25^{+16}_{-4} in the WN, and $2.0^{+4.2}_{-1.5}$ in the EN.

6.1.3. SiO

We used the upper, middle and lower $H^{13}CN$ column densities found for each nucleus, and restricted our parameters to $T_k = 150$ K, $T_{bg} = 45$ K and $\Delta v = 100$ km s^{-1}. The maximum and minimum values of the resultant SiO column density were used to estimate uncertainties. We ran grids for the parameter range n_{H_2} for 10^5–10^7 cm^{-3} in $\log_{10}$ steps of 0.01, while N_{SiO} was varied to include the range permitted by the ratios. This was particularly significant for the 3.5 mm ratio in the EN, where the ratio alone cannot exclude extremely low $[H^{13}CN]/[SiO]$ ratios. We used the $T_B dv$ ratios, excluding the negative components of the SiO(6–5) line. The results for both case 1 and 2 are shown in Figure 14. Numerical results for the SiO fitting are collated in Table 4.

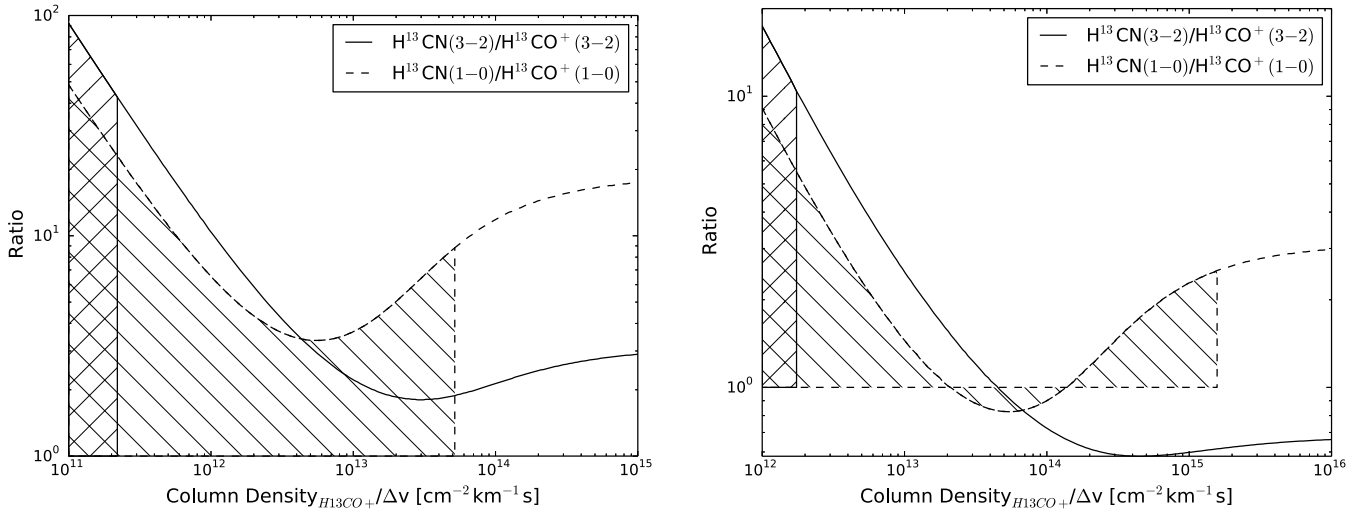

Figure 12. Regions of $H^{13}CO^+$ column density permitted by the lower limit ratios of case 1 in the WN (left) and EN (right). The hashed regions indicate the permitted columns for each ratio assuming $n_{H_2} = 2.1 \times 10^6\,cm^{-3}$. Higher column densities are permitted for lower n_{H_2} values. We find upper limits on the $H^{13}CO^+$ column density of $2 \times 10^{11}\,cm^{-2}\,km^{-1}\,s$ and $2 \times 10^{12}\,cm^{-2}\,km^{-1}\,s$ in the WN and EN respectively.

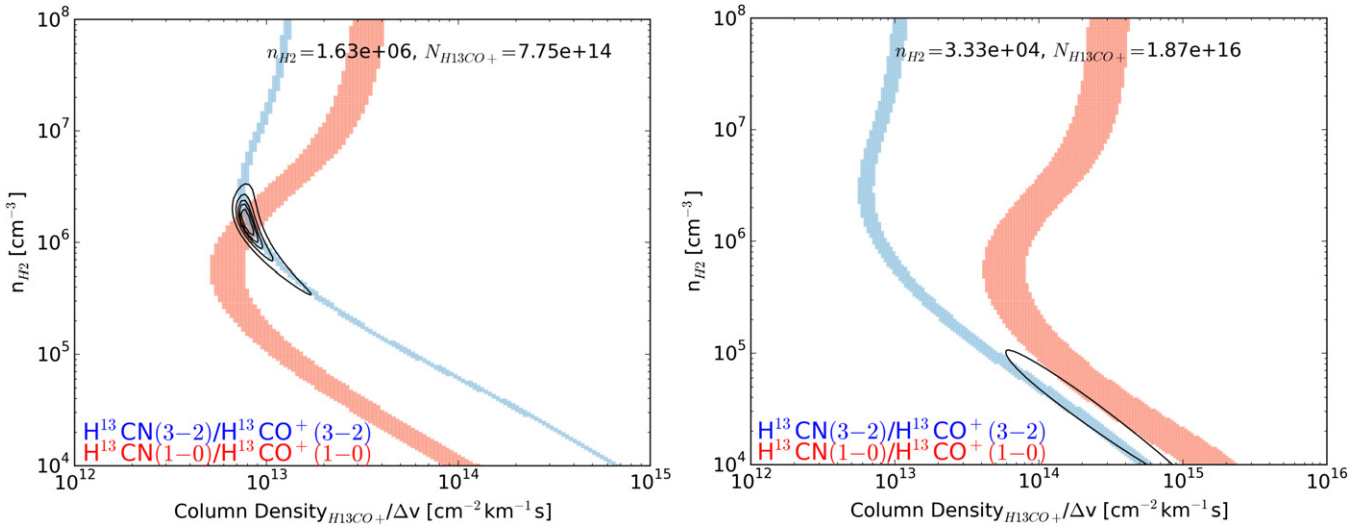

Figure 13. Error regions for the modeled $H^{13}CO^+$ line ratios in the WN (left) and EN (right). χ^2 contours are overlaid at 1, 2, 3, 5, and 10. The minimum χ^2 locations are indicated in the top right corners of the plots. Best fits give an abundance ratio $[H^{13}CN]/[H^{13}CO^+]$ of 25^{+16}_{-4} in the WN, and $2.0^{+4.2}_{-1.5}$ in the EN.

Table 4
Sio Abundance Results

	WN		EN	
	$[H^{13}CN]/[SiO]$	$N_{SiO}/\Delta v$ (10^{13}cm^{-2} km^{-1} s)	$[H^{13}CN]/[SiO]$	$N_{SiO}/\Delta v$ (10^{13}cm^{-2} km^{-1} s)
	Case 1: no $H^{13}CO^+$			
1.2 mm	$3.4^{+1.5}_{-0.8}$	$5.6^{+1.7}_{-1.7}$	$3.3^{+3.8}_{-1.2}$	$5.8^{+3.3}_{-3.1}$
3.5 mm	$0.42^{+0.04}_{-0.05}$	46^{+6}_{-4}	$0.15^{+0.35}_{-0.10}$	130^{+250}_{-90}
Mean[a]	$0.74^{+0.11}_{-0.08}$	$25.5^{+3.8}_{-2.9}$	$0.28^{+0.50}_{-0.20}$	70^{+130}_{-50}
	Case 2: $H^{13}CO^+$			
1.2 mm	$6.4^{+3.9}_{-2.1}$	$3.0^{+1.4}_{-1.1}$	$5.1^{+4.0}_{-1.6}$	$3.7^{+1.7}_{-1.6}$
3.5 mm	$0.47^{+0.05}_{-0.04}$	41^{+4}_{-4}	$0.36^{+0.08}_{-0.22}$	53^{+83}_{-10}
Mean[a]	$0.87^{+0.11}_{-0.10}$	$22.0^{+2.8}_{-2.4}$	$0.67^{+0.99}_{-0.14}$	29^{+42}_{-6}

Note. Since the varied parameter is the SiO column density, the mean here is the arithmetic mean for $N_{SiO}/\Delta v$, and the harmonic mean for the $[H^{13}CN]/[SiO]$ abundance ratio.

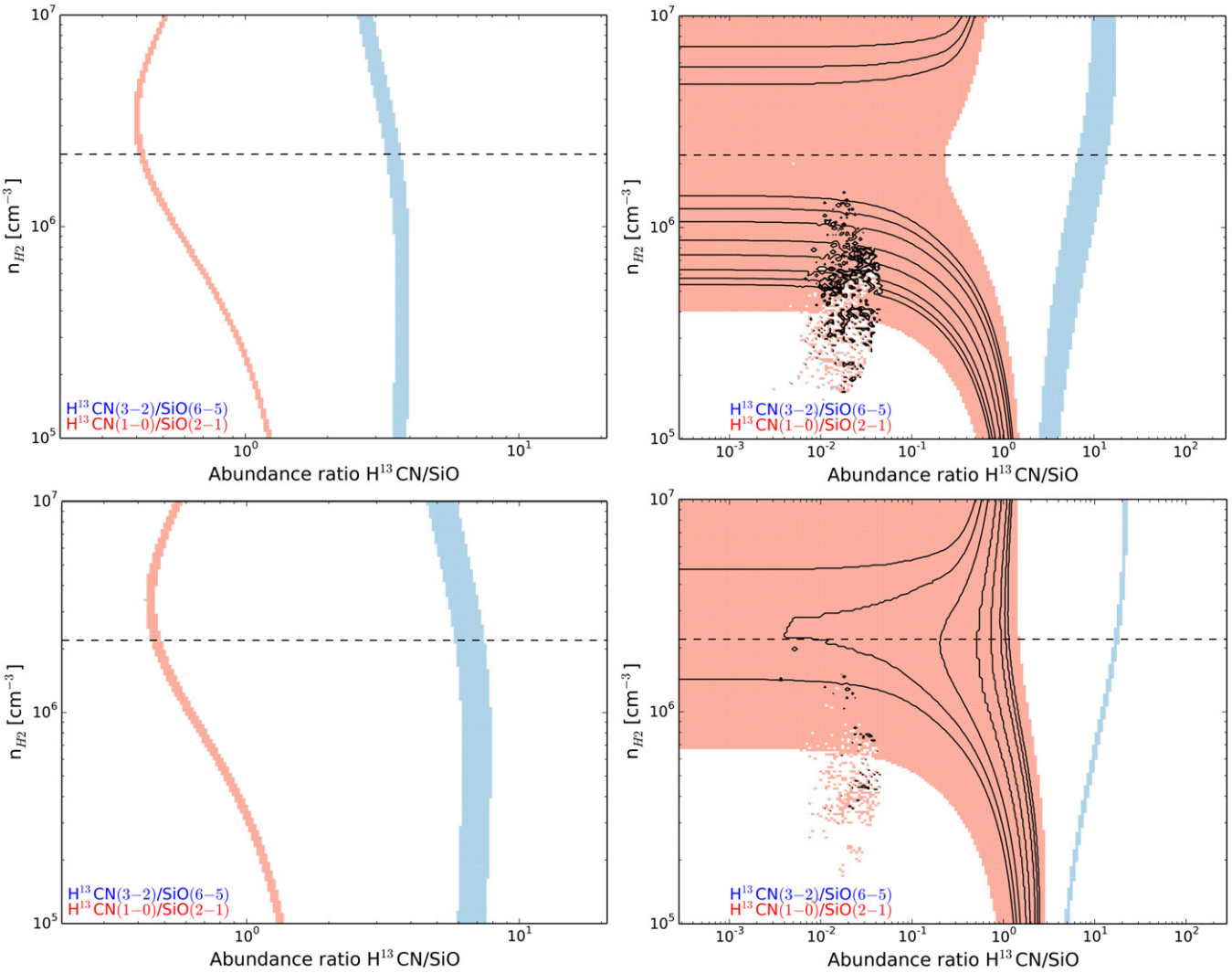

Figure 14. 1σ regions for the modeled [$H^{13}CN$]/[SiO] abundance ratio in the WN (left) and EN (right) for both case 1 (top) and case 2 (bottom). The dashed horizontal line marks the best fitting n_{H_2} from HCN modeling, and the EN plots show the χ^2 contours for the 3.5 mm component at 0.01, 0.1, 0.2, and 0.3. Numerical results of these models are shown in Table 4.

The results for case 1 and case 2 vary as expected, with higher [$H^{13}CN$]/[SiO] ratios for case 2, although the ratios are consistent within uncertainties. We find consistent [$H^{13}CN$]/[SiO] ratios for the two nuclei of $0.74^{+0.11}_{-0.08}$ and $0.28^{+0.50}_{-0.20}$ in the WN and EN respectively for case 1 and $0.87^{+0.11}_{-0.10}$ and $0.67^{+0.99}_{-0.14}$ in the WN and EN respectively for case 2. This would suggest that the elevated [$H^{13}CN$]/[$H^{13}CO^+$] abundance ratio in the WN is due to either a process which is elevating the [$H^{13}CN$] and [SiO] abundances in tandem, or a process which is lowering the [$H^{13}CO^+$] abundance.

6.2. $HC^{15}N$(3–2) or SO(6_6–5_5)?

We attempted to distinguish between $HC^{15}N$(3–2) and SO(6_6–5_5) by using our HCN parameter results as inputs to LVG models. Assuming [HCN]/[$H^{13}CN$] = 60 and [HCN]/[$HC^{15}N$] = 200, we predict an integrated brightness temperature ratio in the WN for $HC^{15}N$(3–2)/$H^{13}CN$(3–2) of 0.4. Using the SO column density from Martín et al. (2011) of $\sim 10 \times 10^{14}$ cm^{-2} the LVG model predicts an integrated ratio SO(6_6–5_5)/$H^{13}CN$(3–2) = 0.006. Our observed value of $\sim$2, suggesting that the spectral feature may be dominated by $HC^{15}N$ and not SO, or really is a blending of the two. However the ^{15}N isotopic abundance is very uncertain, and could be3 $\times$ lower. Furthermore, the beam size of Martín et al. (2011) is almost 300 $\times$ greater than ours: if their observed SO(5_5–4_4) emission is as tightly centered about the nuclei as our SO(6_6–5_5), then their LTE analysis could be heavily affected by beam dilution, underestimating the SO column density. Therefore we cannot exclude either possibility with these results, but if the spectral feature is dominated by $HC^{15}N$(3–2), it is consistent with an abundance ratio [HCN]/[$HC^{15}N$] $\lesssim$ 200.

The results of the above LVG analysis are collated in Table 5, where the results for T_k = 450 K and T_{bg} = 110 K are also shown. We found that while the higher T_k and T_{bg} lowered the absolute abundances by over a dex, the abundance ratios are practically unchanged and are consistent within uncertainties. Our LVG derived abundance ratios therefore appear to be quite robustly determined over a wide range in kinetic temperature. The column densities over Δv and CO and H_2 abundance ratios for our T_k = 150 K and T_{bg} = 45 K results are given in Table 6. The quoted uncertainties are propagated from the LVG modeling; the errors due to the uncertainty in T_k are not included but, as noted previously, could be as large as a dex.

Table 5
Abundance Ratio Comparison for $T_k = 150$ K, $T_{bg} = 45$ K and $T_k = 450$ K, $T_{bg} = 110$ K

	WN		EN	
	$T_k = 150$ K, $T_{bg} = 45$ K			
	$[H^{13}CN]/[H^{13}CO^+]$	$[H^{13}CN]/[SiO]$	$[H^{13}CN]/[H^{13}CO^+]$	$[H^{13}CN]/[SiO]$
Case 1	>950	$0.74^{+0.11}_{-0.08}$	>185	$0.28^{+0.53}_{-0.20}$
Case 2	25^{+16}_{-4}	$0.87^{+0.11}_{-0.10}$	$2.0^{+4.2}_{-1.5}$	$0.67^{+0.99}_{-0.14}$
	$T_k = 450$ K, $T_{bg} = 110$ K			
	$[H^{13}CN]/[H^{13}CO^+]$	$[H^{13}CN]/[SiO]$	$[H^{13}CN]/[H^{13}CO^+]$	$[H^{13}CN]/[SiO]$
Case 1	>640	$0.60^{+0.09}_{-0.07}$	>180	$0.171^{+0.003}_{-0.092}$
Case 2	23^{+17}_{-6}	$0.70^{+1.0}_{-0.09}$	$2.0^{+3.3}_{-1.7}$	$0.42^{+1.60}_{-0.17}$

Table 6
LVG Model Abundance Results

	Column Densities	Abundance Ratios[a]	
	$N_X/\Delta v$ (10^{13} cm^{-2} km^{-1} s)	$[X]/[CO]$[b]	$[X]/[H_2]$[c]
HCN	620^{+160}_{-160}	$2.8^{+0.7}_{-0.7} \times 10^{-3}$	$6.2^{+1.6}_{-1.6} \times 10^{-8}$
$H^{13}CN_{WN}$	19^{+22}_{-10}	$9^{+10}_{-5} \times 10^{-5}$	$1.9^{+2.2}_{-1.0} \times 10^{-9}$
$H^{13}CN_{EN}$	37^{+57}_{-18}	$1.7^{+2.6}_{-0.8} \times 10^{-4}$	$3.7^{+5.7}_{-1.8} \times 10^{-9}$
Case 1: no $H^{13}CO^+$			
$H^{13}CO^+_{WN}$	<0.02	$<9 \times 10^{-8}$	$<2 \times 10^{-12}$
$H^{13}CO^+_{EN}$	<0.2	$<9 \times 10^{-7}$	$<2 \times 10^{-11}$
SiO_{WN}	$25.5^{+3.8}_{-2.9}$	$1.16^{+0.17}_{-0.13} \times 10^{-4}$	$2.55^{+0.38}_{-0.29} \times 10^{-9}$
SiO_{EN}	70^{+130}_{-50}	$3.2^{+5.9}_{-2.3} \times 10^{-4}$	$7^{+13}_{-5} \times 10^{-9}$
Case 2: $H^{13}CO^+$			
$H^{13}CO^+_{WN}$	$0.8^{+0.7}_{-0.4}$	$3.6^{+3.2}_{-1.8} \times 10^{-6}$	$8^{+7}_{-4} \times 10^{-11}$
$H^{13}CO^+_{EN}$	19^{+66}_{-13}	$9^{+30}_{-6} \times 10^{-5}$	$1.9^{+6.6}_{-1.3} \times 10^{-9}$
SiO_{WN}	$22.0^{+2.8}_{-2.4}$	$1.00^{+0.13}_{-0.11} \times 10^{-4}$	$2.20^{+0.28}_{-0.24} \times 10^{-9}$
SiO_{EN}	29^{+42}_{-6}	$1.32^{+1.91}_{-0.27} \times 10^{-4}$	$2.9^{+4.2}_{-0.6} \times 10^{-9}$

Notes.
[a] Assuming $\Delta v = 100$ km s^{-1}.
[b] CO column densities are taken from the maximum likelihood estimates of Rangwala et al. (2011) as the sum of the cold and hot phase columns: $N_{CO} = 2.2 \times 10^{20}$ cm^{-2}, i.e., $[CO]/[H_2] = 2.2 \times 10^{-5}$.
[c] For $N_{H_2} = 1 \times 10^{25}$ cm^{-2}.

7. DISCUSSION

7.1. Chemical Evidence for an AGN in the WN?

An increasingly common strategy to identify the AGN contribution to the bolometric luminosities of ULIRGs has been to study their HCN/HCO$^+$ integrated intensity ratios (Kohno et al. 2001; Imanishi et al. 2006; Papadopoulos 2007; Krips et al. 2008; Imanishi et al. 2009). The general trend, as described by Krips et al. (2008) is that of increasing $(J \rightarrow J-1)/(J-1 \rightarrow J-2)$ intensity ratios for HCN and HCO$^+$ transitions, as well as a decreasing HCN$(J \rightarrow J-1)$/HCO$^+(J \rightarrow J-1)$ ratio, for an increased starburst contribution. These ratios seem to follow a trend from PDR-dominated emission in starbursts, to XDR-dominated emission in the most AGN-dominated galaxies. Krips et al. (2008) single dish analysis of Arp 220 within this framework found it to not fit well with any of their other galaxies (starburst (SB)-dominated, SB–AGN composite, or AGN-dominated), but that it was closest to NGC 6951, an SB-dominated galaxy with a weak AGN contribution. This possibility of an AGN has been challenged however by Costagliola et al. (2011), who found strong emission from HC_3N, a molecule thought to be readily destroyed in even hard UV environments, let alone XDRs, associated with the highest HCN/HCO$^+$ ratios. Instead, hot core chemistry models (Bayet et al. 2006, 2008) simultaneously explain both decreased HCO$^+$ and elevated HC_3N. Throughout all of this however, we must remember that we are averaging over the entire nuclear disk in our beam, covering dense clouds, diffuse gas, hot cores, PDRs and XDRs, all with potentially large cosmic ray contributions (evident from excited OH$^+$ emission González-Alfonso et al. 2013), due to the observed supernova rate of ∼4 a year, so the two phase LVG model we employ for $H^{13}CN$ and $H^{13}CO^+$ will be an extreme simplification.

Most recently, Martín et al. (2014) have suggested that elevated [HCN]/[HCO$^+$] abundance ratios are due not to XDR or PDR chemistry, but rather extensive shock chemistry in the turbulent regions of the CND. This would be consistent with the kinematics of the our 1.2 mm $H^{13}CN$ and SiO lines in the WN, which suggest an outflow originating close to the continuum center, as well as the high densities and kinetic temperatures of the LVG fits. García-Burillo et al. (2014) observed an AGN-driven molecular outflow in NGC 1068 with an elevated HCN(4–3)/HCO$^+$(4–3) brightness temperature ratio (∼2.5) in the regions immediately surrounding the AGN (within 140 pc), but significantly lower (∼1.3) directly toward the AGN. This is consistent with the elevated HCN/HCO$^+$ ratios being caused by AGN-driven mechanically dominated regions (MDRs), and not XDRs.

Meijerink & Spaans (2005); Meijerink et al. (2007, 2011) extensively modeled PDRs and XDRs over a range of densities and ionization rates in an attempt to identify unique tracers of the two regions. For the high density environment of the HCN our $[H^{13}CN]/[H^{13}CO^+]$ ratios are consistent with both PDR and XDR results. Additionally, Meijerink et al. (2011) studied the effects of cosmic rays and mechanical heating, and found evidence that strong mechanical heating can lead to very elevated HCN and HNC abundances (10^{-4} and 10^{-6} respectively) and low [HNC]/[HCN] ratios (1–0.01). While our abundances are very uncertain, the $HN^{13}C(3–2)/H^{13}CN(3–2)$ line integrated ratios of 0.71 ± 0.04 and 0.66 ± 0.04 are consistent with shock-heating, but not with high density XDRs.

Our LVG derived abundance ratios in case 1 and case 2 are shown in Figure 15. We omit the dependent ratio $[SiO]/[H^{13}CO^+]$ from the plot as it can be calculated trivially from the other two, and lying so close to $[H^{13}CN]/[H^{13}CO^+]$ including it would significantly obfuscate the figure. We find an elevated $[H^{13}CN]/[H^{13}CO^+]$ ratio in the WN in both case 1 and case

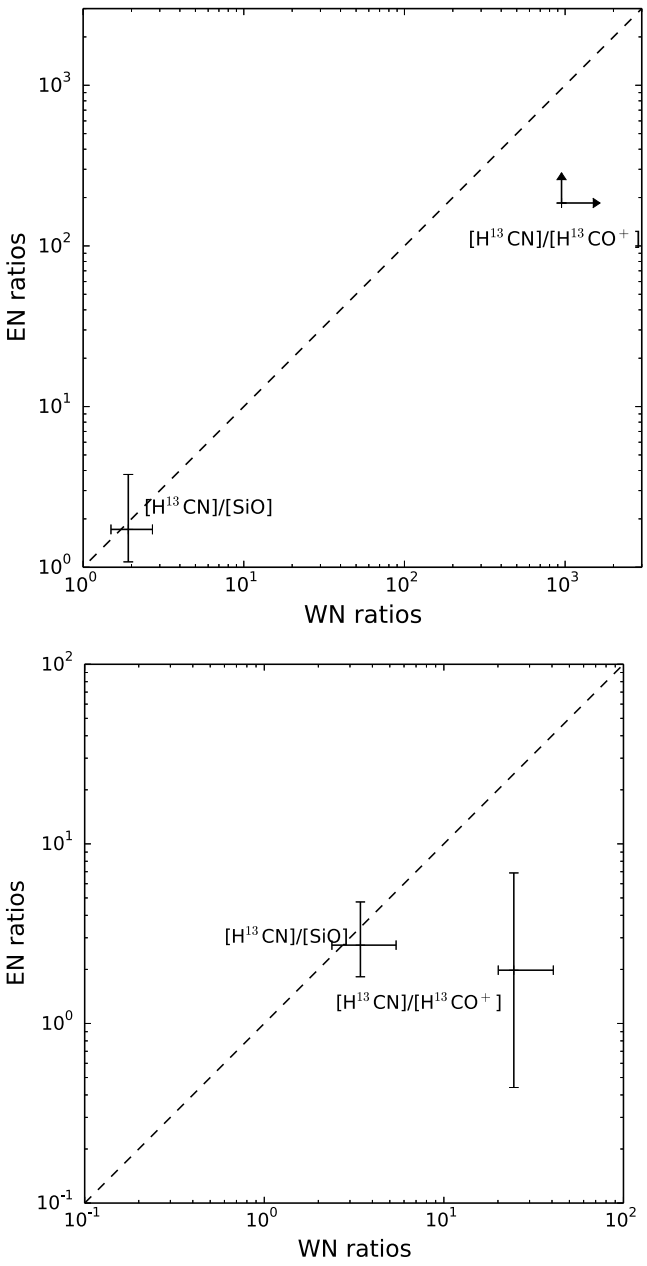

Figure 15. LVG derived abundance ratios $[H^{13}CN]/[H^{13}CO^+]$ and $[H^{13}CN]/[SiO]$ in the two nuclei, for case 1 (top) and case 2 (bottom). Both show a clear distinction between the two nuclei with $[H^{13}CN]/[H^{13}CO^+]$ elevated in the WN. The dependent ratio $[SiO]/[H^{13}CO^+]$ is similarly elevated in the WN.

2. The case 1 ratios are unphysically high for the $H^{13}CN$ derived n_{H_2}, but for $5 \times 10^4\,cm^{-3}$ the ratio of 44 in the WN is entirely physical. The case 2 ratios, based on the upper limit of the $H^{13}CO^+$ contribution, yield lower limits on the $[H^{13}CN]/[H^{13}CO^+]$ abundance ratios. Therefore the case 2 ratios of 25^{+16}_{-4} and $2.0^{+4.2}_{-1.5}$ in the WN and EN respectively, confirm that the ratio is elevated in the WN not only with respect to the EN, but also with respect to the starburst dominated cases of Krips et al. (2008). We find a conservative (3σ) lower limit on the ratios of 11 and 0.10 in the WN and EN respectively. The WN $[H^{13}CN]/[H^{13}CO^+]$ is consistent with $[HCN]/[HCO^+]$ ratios found by Krips et al. (2008), who found ratios between 0.01 and 50 (for starburst and AGN-dominated galaxies, respectively). Empirically therefore, our observations suggest that there is an energetically significant AGN in the WN of Arp 220, while the EN is powered predominantly by a starburst. This is consistent with Engel et al. (2011) who found that the 10 Myr old starburst is more prevalent in the EN.

We note that it is entirely possible that we have case 1 in the WN and case 2 in the EN. The evidence for this is largely the kinematic similarity with HCO^+(3–2) in the WN (which is far more convincing than in the EN) combined with the northward offset of the case 2 $H^{13}CO^+$(3–2) line in the EN, which is hard to explain in case 2 but in case 1 implies a symmetry in the SiO outflow with $\pm 500\,km\,s^{-1}$ components. In the EN however the kinematic comparison to Sa09 makes it harder to exclude all $H^{13}CO^+$(3–2) emission, favoring case 2.

The comparison with Krips et al. (2008) is entirely empirical, and cannot distinguish between an XDR and an MDR. Whether the trend of increasing $[HCN]/[HCO^+]$ ratio with increasing AGN contribution is driven by an XDR or MDR does not affect the conclusion that an AGN is likely present in the WN. Nevertheless, the P Cygni profiles, high velocities, high gas kinetic temperatures and densities, as well as the low $HN^{13}C(3–2)/H^{13}CN(3–2)$ line integrated ratios, point toward extensive shock heating and shock chemistry in Arp 220.

7.2. Shocked Gas in a Molecular Outflow?—the Origin of the Species

Based on similar blueshifted absorption in *both* nuclei despite their misaligned disks, Sa09 concluded that the P Cygni profiles were evidence of radial outflow in most directions, and not bound non-circular motion along the line of sight. Herschel observations have revealed P Cygni profiles in OH^+, H_2O and HF (Rangwala et al. 2011), as well as high velocity redward components to the OH and H_2O lines (GA12). The embedded P Cygni profile of $H^{13}CN$(3–2) and the P Cygni profile of SiO(6–5), including the high velocity absorption (seen out to $-600\,km\,s^{-1}$ and troughing about $-500\,km\,s^{-1}$) add to the evidence for an outflow from the Arp 220 WN. Furthermore, the high abundance of SiO and the high $[H^{13}CN]/[H^{13}CO^+]$ ratio suggests that this outflow contains shocked gas.

Notably, the high velocity blueshifted absorption seen in HCO^+(3–2) (Sa09) and SiO(6–5) has no analogue in blueshifted emission in any observed species, although Sa09 did see $\sim 500\,km\,s^{-1}$ redshifted components in both HCO^+(3–2) and CO(3–2). As these are high-J transitions they require populated $J = 2$ and $J = 5$ levels respectively to absorb the continuum: future high resolution observations of SiO(5–4) may reveal high velocity emission.

As is discussed in detail in Section 4, we suggest that $H^{13}CN$, with the small P Cygni component is prevalent throughout the CND, but also elevated in the outflow (e.g., Martín et al. 2014). SiO is almost exclusively present in the outflow, with a small CND component. $H^{13}CO^+$ would be present predominantly in the outflow (evidenced by the line profiles of Sa09), but its abundance is heavily suppressed.

Sakamoto & Scoville (1999) found, on the basis of 0.″5 CO(2–1) observations, two counter rotating nuclear discs, each $\sim 100\,pc$ in diameter, embedded in a much larger rotating outer disk. They base the orientation of the WN disk (near-side southward) on the sharp falloff of light in NICMOS images. More recent work (Wilson et al. 2014) has constrained the continuum sizes to be $76 \times <70\,pc$ for the WN at 53° inclination and $123 \times 79\,pc$ for the EN. The bipolar outflow model presented below requires that the WN disk be oriented near-side northward.

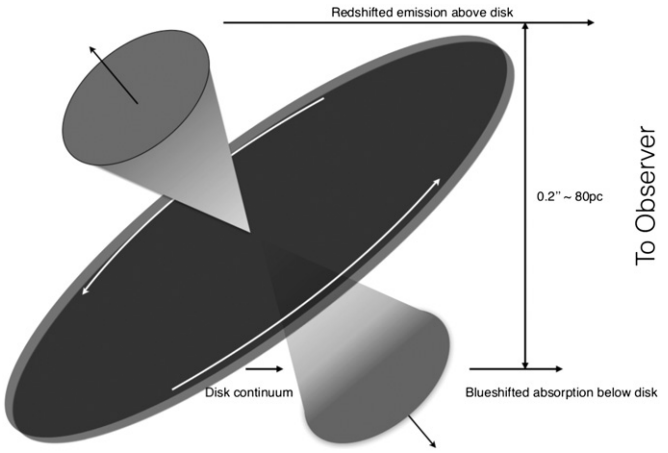

Figure 16. Outline of a possible geometry for Arp 220 WN. The highly schematic diagram shows the bipolar outflow scenario, where the north–south offsets of the emission and absorption peaks respectively is explained by a combination of dust opacity and the line-of-sight column density being at a maximum away from the continuum center. Redshifted emission, behind the disk, is significantly attenuated close to the continuum center, but as it flows north and away from the disk is increasingly transmitted as thickness of intervening dust decreases. At ∼40 pc north the light reaching us is maximal: farther north the emitting column is decreasing or the excitation conditions are changing faster than transmitted fraction is increasing. South of the continuum center, the absorption peaks at ∼−40 pc because while the line-of-sight column continues to increase, the continuum emission falls off rapidly farther south.

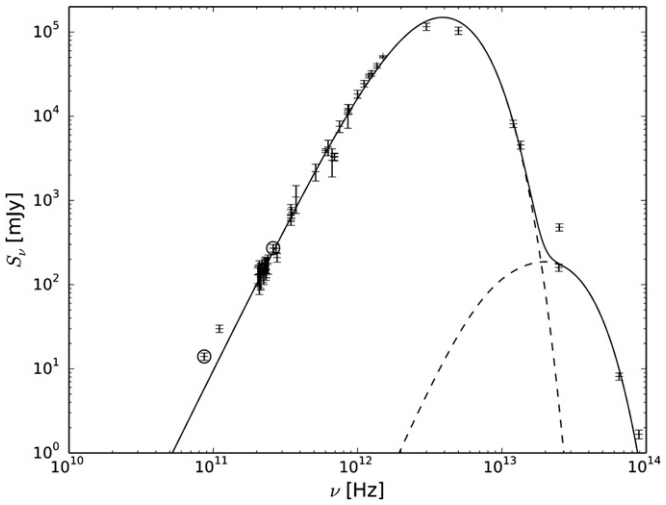

Figure 17. Continuum fluxes for Arp 220 from Table 7, Martín et al. (2011), Rangwala et al. (2011) and *WISE* data. We fit the data with two gray bodies. Our continuum measurements are circled. We find best fit parameters $\nu_{0,1} = 1.6 \times 10^3$ GHz (190 μm), $\beta_1 = 1.5$, $A_1 = 4.9 \times 10^{-32}$ mJy Hz^{-3} and $T_1 = 62$ K for the main component, and $\nu_{0,2} = 1.0$ GHz, $\beta_2 = 1.6$, $A_2 = 3.8 \times 10^{-37}$ mJy Hz^{-3} and $T_2 = 340$ K for the hotter component.

In stellar P Cygni profiles, the red emission and blue absorption originate along the same line of sight with gas leaving the star roughly isotropically. We see blue absorption across all of the southern half of the WN, i.e., south of the continuum peak, but it peaks ∼40 pc south, while the emission peaks ∼40 pc north. In the 0 km s^{-1} channel of Figure 8 the offset is even greater. This would suggest that while SiO is present mainly in the outflow, there is a disk component which is obscuring the outflow close to the continuum center. While this could, hypothetically, be due to dust preferentially obscuring low velocity SiO, it is hard to envision the geometry of such a system that is consistent with the spatial profiles at higher velocities.

We propose an outflow geometry similar to the one shown in Figure 16. In this toy model, an outflow leaves the nuclear disk roughly perpendicularly (∼37° to the line of sight). As it advances it shocks the dusty medium, liberating SiO through grain sputtering. This leads to a maximum column depth being obtained offset from the disk center. Since the SiO(6–5) line is only just optically thick, the emission and absorption peaks coincide with the regions of maximum column depth, so we see emission and absorption peaks offset from one another and from the continuum. North of the disk, the redshifted emission behind the disk is attenuated by the optically thick dust between the outflow and the observer. As it flows north there is less intervening dust, increasing the transmitted fraction until there is a peak at ∼40 pc north. Beyond this point, either due to column density or the gas properties the emission decreases rapidly. South of the disk, the fraction of the continuum absorbed by the outflow increases as the column density increases, until it reaches the edge of the disk and the continuum falls off rapidly, leaving nothing to be absorbed.

The requirement that the column density increases away from the continuum center, which by number conservation requires SiO to be either swept up or sputtered from dust, would invalidate our abundance estimates of SiO as the SiO emission would be offset from the peak H_2 column density, implying a much greater SiO abundance than we found in Section 6.1. GA12 found 3×10^9 $M_\odot$ of dust in an optically thin, extended halo (650 pc diameter) about both nuclei, confirming that there is dust available outside of the WN for this model.

The lack of a P Cygni profile in the SiO(2–1) line can be readily explained by the fainter continuum at 3.5 mm as well as both the dust and the SiO line becoming optically thin at these longer wavelengths.

Sa09 noted that the low velocity of the main absorption HCO^+(3–2) is evidence that any outflow is not driven by an AGN, but rather is either directly related to the nuclear starburst or to the merger super-wind. We see this absorption in SiO(6–5) and $H^{13}CN$(3–2), but given the high velocity SiO components in both HCO^+ and SiO and in light of the chemical evidence presented above, it could be that the outflow is only just beginning to be launched from the luminous core (be it starburst or AGN), and so has not yet all been accelerated to the velocities seen in more extreme outflows (e.g., Cicone et al. 2014). For our proposed geometry projection effects are insignificant: correcting for the ∼40° angle of the outflow to the line of site only increases the velocities by a factor of 1.15. We propose that the molecular outflow is driven by a nascent/heavily obscured AGN. The geometry of the proposed outflow prohibits an upper limit on the outflow age, it does provide a lower limit of $\sim 6 \times 10^4$ yr, assuming that the outflow was launched at ∼500 km s^{-1} and the 150 km s^{-1} absorption is from gas which has been slowed by shocks after escaping the WN. If, as we propose in the chemical discussion above, we have case 1 in the WN, then the SiO(6–5) velocity slice is almost symmetric about −25 km s^{-1}, with emission and absorption extending out to + and −550 km s^{-1} respectively.

The outflow structure will be investigated further in a future paper, where we will use H_2 kinematic models, and SiO shock chemistry models to better interpret these results. The profusion of supernova remnants and explosions observed in the radio Batejat et al. (2011) suggests that shocked gas and mechanically sputtered dust could be extremely prevalent in Arp 220, and LVG codes, even with the addition of mid-IR pumping, may

be insufficient to accurately model the abundances in shock-chemistry dominated regions.

7.3. SiO Abundance

Our intermediate SiO abundance is three orders of magnitude higher than would be expected for quiescent, Galactic, gas (Martin-Pintado 1992), but one lower than seen in Galactic shocks. However, the extremely dusty Arp 220 may have a higher quiescent gas phase silicate abundance than the Milky Way. Downes & Eckart (2007) found that if there is a buried AGN at the center of the WN it must be surrounded by a very thick and dusty torus.

Our abundances are consistent with other extragalactic studies of SiO(2–1) and $H^{13}CO^+$(1–0). García-Burillo et al. (2000); García-Burillo et al. (2001); García-Burillo et al. (2010) and Usero et al. (2006) found SiO abundances in the range 10^{-9}–10^{-10} in the CNDs of NGC 253, M 82, NGC 1068 and IC 342 respectively. These SiO abundances were derived from the SiO/$H^{13}CO^+$ ratios and assumed $H^{13}CO^+$ abundances. For NGC 1068 the abundance was also found from the SiO(3–2)/SiO(2–1) ratio and was consistent with that derived from an assumed $H^{13}CO^+$ abundance. In NGC 253 the abundance increases from 1×10^{-10} in the central nuclear disk to 5×10^{-10} in the nuclear outflow. M 82 has a particularly complex morphology with a low abundance in the galactic disk (1×10^{-11}), increasing to 1×10^{-10} in a supershell and to 1×10^{-9} in a silicate chimney. NGC 1068 has abundances in the range 1–5 $\times 10^{-9}$ in the CND, while IC 342 has a CND abundance of 2×10^{-10} but this rises to 1×10^{-9} in the spiral arms. Here, in case 2, we find abundances of $2.2^{+0.28}_{-0.24} \times 10^{-9}$ and $2.9^{+4.2}_{-0.6} \times 10^{-9}$ in the WN and EN CNDs respectively. These uncertainties are nominal, assuming the $T_k = 150$ K, $T_{bg} = 45$ K and $n_{H_2} = 2.1 \times 10^6$ cm^{-3}. For different conditions the abundances can vary by more than a dex.

Our SiO column density is $\sim$2–7 $\times 10^{16}$ cm^{-2}, while Martín et al. (2011) found, based on LTE modeling of the SiO(5–4) transition, $\sim 1 \times 10^{14}$ cm^{-2}, 100 $\times$ lower. This is particularly important since the absorption we see in the SiO(6–5) line requires that the $J = 5$ level is populated. This difference may be due to the large beam (8.″5 $\times$ 7.″0, 300 $\times$ the area of our beam) of the SMA configuration used for the line survey of Martín et al. (2011). If the SiO emission is more compact than other lines this would lead to significant dilution, and a reduced column estimate. Higher resolution observations of the SiO(5–4) line combined with radiative excitation modeling are needed to obtain a better estimate of the column density.

7.4. The Dense Gas Fraction

Engel et al. (2011) found a dynamical mass within 100 pc of the WN of 6.3×10^9 $M_\odot$. Using the H_2 density found from our LVG models, including a factor of 1.3 for helium and assuming a single core and a WN disk $75 \times 70 \times 10$ pc, implies a gas mass $\gtrsim 1.7 \times 10^{10}$ $M_\odot$, about 3 $\times$ the dynamical mass, implying that the HCN and $H^{13}CN$ disk emission is from multiple small, dense cores distributed across the nuclear disk. Repeating this exercise for the EN, dynamical mass 5.8×10^9 $M_\odot$ leads to the same conclusion. Downes & Solomon (1998) suggested gas masses of 6×10^8 $M_\odot$ and 1.1×10^9 $M_\odot$ for the WN and EN respectively, which would suggest that the HCN dense cores cannot have a filling factor greater than 0.1 in the WN disk.

A shell of gas about a single "hot core," powered by the 5 pc radius 400 K dust continuum found by GA12, is also possible on dynamical grounds, with a shell 0.1 pc thick having a mass $\sim 3 \times 10^6$ $M_\odot$.

7.5. The HNC/HCN Ratio

Aalto et al. (2007) found the line integrated brightness temperature ratio HNC(3–2)/HCN(3–2) = 1.9 ± 0.3. This was explained to be due to either mid-IR pumping, where HNC is preferentially pumped over HCN by two orders of magnitude, or XDR chemical effects. We found $T_B dv$ ratios for $HN^{13}C$(3–2)/$H^{13}CN$(3–2) = 0.71 ± 0.04 in the WN, and 0.66 ± 0.04 in the EN, and $T_{B,peak}$ ratios of 0.689 ± 0.023 and 0.453 ± 0.010 in the WN and EN respectively. Both measures present $HN^{13}C$ as under-luminous with respect to $H^{13}CN$.

The WN value is uncertain due to the missing blue component of the line, estimated generously to be $\lesssim$25% but not included in our results, but even allowing for a missing 40% on the $HN^{13}C$(3–2) line the ratio is still $\sim$1, as a very generous upper limit. The EN value on the other hand is much more reliable, due to the additional redshift of the EN shifting almost all of the line into our spectrum. This discrepancy between the optically thick HNC/HCN and their much less optically thick ^{13}C isotopologues would suggest that the significantly different ratio is due to optical depth effects. Not only can we see deeper into the high density environments, but the molecules will be less self-shielded against mid-IR pumping. This would lead to us seeing a greater fraction of the HNC and HCN which is hidden in dense cores, and protected against mid-IR pumping. In the "raisin roll" model of Aalto et al. (2007), the mid-IR field in Arp 220 drives widespread HNC emission while the optical depth of the HCN emission, primarily from dense cores, reduces the observed HCN intensity below what would be expected from its true [HNC]/[HCN] abundance ratio and the HNC intensity, leading to the high observed HNC/HCN ratio. When we observe the isotopologues however, we see a truer representation of the [HNC]/[HCN] abundance ratio as we no longer have optically thick thermal emission from the dense cores.

We note that there might be some concern with extending the logic applicable to the carbon-12 isotopologues to the carbon-13 isotopologues. Measurements of $HN^{13}C$ transitions are few and far between, but data from Harris et al. (2008), and the fact that the energy of the first excited bending mode (which is relevant for mid-IR pumping) has an energy proportional to $\rho^{-0.5}$ where ρ is the reduced mass, suggest any differences should be on the order of 1%. Any arguments based on the susceptibility to mid-IR pumping applicable to the HNC/HCN ratio should also apply to the $HN^{13}C/H^{13}CN$ ratio.

8. CONCLUSIONS

We have presented spectral imaging of the prototypical ULIRG Arp 220 at 3.5 mm and 1.2 mm from the PdBI. We observe complex molecular lines including $H^{13}CN$, $H^{13}CO^+$, $HN^{13}C$, and SiO. These results are consistent with previous millimetre studies of Arp 220, while also revealign shocked gas in the molecular outflow, building upon the molecular outflow observed by Sa09 in HCO^+. A chemical and kinematic analysis suggests that we have non-detections of $H^{13}CO^+$ in the WN, but detections in the EN. Further high resolution work is needed to study the kinematically complex gas in Arp 220, in particular the SiO transition ladder at frequencies uncontaminated by $H^{13}CO^+$. Observations resolving the molecular emission within the disks are essential, and would allow us to identify whether the emission from different species is segregated to the extent

we propose above. Chemical shock models, combined with kinematic and radiative transfer models may be able to shed more light on the environments traced by the complex line profiles we have observed.

1. We have used HCN(3–2) and HCN(1–0) single dish data from the literature and our $H^{13}CN$(3–2) and $H^{13}CN$(1–0) interferometric data with LVG models to constrain the HCN environment in Arp 220, finding dense ($n_{H_2} = 2.1 \pm 0.6 \times 10^6\,cm^{-3}$), hot ($T_k = 150$–$450\,K$) gas.
2. Working in two limiting cases, where we attribute the reddest components of fitted line profiles to either SiO or $H^{13}CO^+$, we find significant chemical differences between the two nuclei, as well as an elevated $[H^{13}CN]/[H^{13}CO^+]$ abundance ratio, in both cases. The lowest $[H^{13}CN]/[H^{13}CO^+]$ abundance ratios correspond to the case where the line component is attributed to $H^{13}CO^+$, and we find abundance ratios $[H^{13}CN]/[SiO] = 0.87^{+0.11}_{-0.10}$ and $0.67^{+0.09}_{-0.14}$ and $[H^{13}CN]/[H^{13}CO^+] = 25^{+16}_{-4}$ and $2.0^{+4.2}_{-1.5}$ in the WN and EN respectively. Therefore the lower limit on the $[H^{13}CN]/[H^{13}CO^+]$ abundance ratios, in the limit of a maximal $H^{13}CO^+$ contribution, are 11 and 0.10 in the WN and EN respectively. If, as we believe is more likely, case 1 (no $H^{13}CO^+$ detections) is a more accurate description of the WN the $[H^{13}CN]/[H^{13}CO^+]$ abundance ratio is significantly larger, most likely >50.
3. The elevated $[H^{13}CN]/[H^{13}CO^+]$ ratio in the WN, compared to the EN and to SB galaxies, suggests (empirically) an energetically significant AGN contribution to the WN luminosity.
4. We find a "normal" (0.1–1.0) brightness temperature ratio for $HN^{13}C(3–2)/H^{13}CN(3–2)$ in both nuclei, suggesting that the elevated HNC/HCN intensity ratio seen by Aalto et al. (2007) is due predominantly to mid-IR pumping, and not an XDR. Combined with the evidence for an AGN, this implies extensive mechanical heating and shock chemistry in Arp 220.
5. We suggest that HCO^+, SiO(6–5) and a fraction of $H^{13}CN$(3–2) are tracing a dense molecular outflow with a large shocked component, and present a toy model geometry which can explain the north–south offset we observe in the SiO(6–5) emission and absorption, which independently reproduces the size of the WN continuum source seen by Wilson et al. (2014).

We thank the anonymous referee their extensive and patient comments, which greatly improved this paper. This research is supported by an STFC PhD studentship. A.U. and P.P. acknowledge support from Spanish grants AYA2012-32295 and FIS2012-32096. T.R.G. acknowledges support from an STFC Advanced Fellowship. S.G.B. acknowledges support from Spanish grants AYA2010-15169 and AYA2012-32295 and from the Junta de Andalucia through TIC-114 and the Excellence Project P08-TIC-03531. A.F. and S.G.B. acknowledge support from Spanish MICIN program CONSOLIDER IMAGENIO 2010 under grant "ASTROMOL" (ref. CSD2009-00038). E.G.A. is a Research Associate at the Harvard-Smithsonian CfA, and thanks the Spanish Ministerio de Economía-Competitividad for support under projects AYA2010-21697-C05-0 and FIS2012-39162-C06-01. Basic research in IR and millimetre wave astronomy at NRL is funded by the US ONR. We thank Kazushi Sakamoto for kindly providing the HCO^+(3–2) spectrum used in Figure 6. We would also like to thank S. Viti, M. Matsura, and Z. Zhang for informative and productive discussions. This work was based on observations carried out with the IRAM PdBI, supported by INSU/CNRS (France), MPG (Germany), and IGN (Spain), and includes observations made with the NASA/ESA *Hubble Space Telescope*, and obtained from the Hubble Legacy Archive, which is a collaboration between the Space Telescope Science Institute (STScI/NASA), the Space Telescope European Coordinating Facility (ST-ECF/ESA) and the Canadian Astronomy Data Centre (CADC/NRC/CSA). This publication also makes use of data products from the *Wide-field Infrared Survey Explorer*, which is a joint project of the University of California, Los Angeles, and the Jet Propulsion Laboratory/California Institute of Technology, funded by the National Aeronautics and Space Administration.

APPENDIX A
CONTINUUM ANALYSIS

The GILDAS task UV_FIT was used to fit two elliptical Gaussians to the 1.2 mm and 3.5 mm continuum UV tables. Elliptical Gaussians were chosen to facilitate meaningful comparisons with the literature. These produced good fits, with flux densities consistent with those obtained from the imaged data. Elliptical disks fit the data with the same rms. error, while point sources provide inferior fits. The residual UV table, after subtraction of the fitted components, was imaged and is consistent with noise. The peak intensity in the imaged residual data cube is 4% of that of the imaged continuum, at the same level as the main beam side lobes, and is not associated with any structure in the map. The fitted parameters, with nominal errors, are presented in Table 7, along with comparable continuum measurements from the literature.

A.1. Synchrotron Subtraction

Norris (1988) and Scoville et al. (1991) found radio synchrotron emission of 36 mJy at 1.3 cm with a spectral index of −0.75. We therefore predict a synchrotron flux density of 14 ± 1 mJy for the two nuclei combined at 3.5 mm and 6 ± 1 mJy at 1.2 mm, giving combined thermal flux densities of 14 ± 2 mJy and 265 ± 20 mJy at 3.5 mm and 1.2 mm respectively. Assuming the same non-thermal/thermal flux density ratio for both nuclei we obtain 8 mJy and 6 mJy for the WN and EN respectively at 3.5 mm and 196 mJy and 69 mJy for the WN and EN respectively at 1.2 mm (Table 7). The 1.2 mm non-thermal flux density is much less than the error in the absolute flux calibration.

A.2. SED Fitting

Using data from the literature including the fluxes in Table 7, Eales et al. (1989) and Rangwala et al. (2011), as well as *Wide-field Infrared Survey Explorer* (*WISE*) measurements of Arp 220, we fitted two gray body models to the SED (Figure 17). The *WISE* flux densities were corrected assuming a 100 K blackbody, as per Wright et al. (2010). We fitted the function:

$$S_{i,\nu} = \left(1 - e^{-\left(\frac{\nu}{\nu_{0,i}}\right)^{\beta_i}}\right) \frac{A_i \nu^3}{e^{\frac{h\nu}{kT_i}} - 1}, \quad \text{(A1)}$$

$$S_\nu = S_{1,\nu} + S_{2,\nu}, \quad \text{(A2)}$$

where ν_0 is the turnover frequency where the dust becomes optically thin, β is the dust emissivity spectral index, T is the dust

Table 7
Continuum Data for Arp 220 in the Millimeter Regime

Source	ν_0 (GHz)	R.A.	Decl.	Size[a] (arcsec)	S_ν[b] (mJy)
This work: WN	86.6	$15^h34^m57^s23$	$23°30'11''50$	$0.53(0.06) \times 0.27(0.05)$	$17(8) \pm 2$
This work: EN		$15^h34^m57^s30$	$23°30'11''32$	$0.43(0.09) \times 0.32(0.07)$	$11(6) \pm 1$
Scoville et al. (1991): both	110.3	...	...	...	30 ± 3
Downes & Eckart (2007): WN	230	$15^h34^m57^s2226$	$23°30'11''46$	0.19×0.13	106 ± 2
Scoville et al. (1997): both	229.4	...	...	1.07×0.63	192 ± 20
This work: WN	260	$15^h34^m57^s22$	$23°30'11''50$	$0.194(0.004) \times 0.1546(0.0021)$	$200(196) \pm 20$
This work: EN		$15^h34^m57^s29$	$23°30'11''34$	$0.258(0.008) \times 0.183(0.007)$	$71(69) \pm 7$
Sa09: WN	273	...	...	...	200 ± 20
Sa09: EN					70 ± 7
Aalto et al. (2009):WN	277	$15^h34^m57^s230$	$23°30'11''50$	...	152 ± 19
Aalto et al. (2009):EN		$15^h34^m57^s310$	$23°30'11''40$	...	57.6 ± 16
Sakamoto et al. (2008): WN	344.6	$15^h34^m57^s215$	$23°30'11''45$	0.28×0.22	380 ± 60
	349.6			0.16×0.13	360 ± 50
Sakamoto et al. (2008): EN	344.6	$15^h34^m57^s285$	$23°30'11''27$	0.31×0.25	200 ± 30
	349.6			0.27×0.14	190 ± 30
Wilson et al. (2014): WN	691	$15^h34^m57^s22$	$23°30'11''5$	$0.21 \times \leqslant 0.19$	1810 ± 270
Wilson et al. (2014): EN		$15^h34^m57^s29$	$23°30'11''3$	0.34×0.2	1510 ± 230

Notes. Data from Martín et al. (2011) are not included as the resolution of the observations precludes individual nuclear size or position measurements.
[a] Numbers in parenthesis are the nominal uncertainties from UV fitting.
[b] Numbers in parenthesis are the estimated synchrotron subtracted flux densities. The errors are dominated by the 10% estimated uncertainty in the absolute flux calibration.

temperature and A is an absolute normalization. We performed a naturally weighted fit of these 8 free parameters to our SED, finding $\nu_{0,1} = 1.6 \times 10^3$ GHz (190 μm), $\beta_1 = 1.5$, $A_1 = 4.9 \times 10^{-32}$ mJy Hz^{-3} and $T_1 = 62$ K for the main component, and $\nu_{0,2} = 1.0$ GHz, $\beta_2 = 1.6$, $A_2 = 3.8 \times 10^{-37}$ mJy Hz^{-3} and $T_2 = 340$ K. This fit has a reduced χ^2 (45 degrees of freedom) of 6.8. We note that $\nu_{0,2}$ is unphysically low, suggesting a blackbody spectrum. This should not be interpreted literally, since we are combining four known dust components (GA12) into a simple 2 element model. As we are only interested in $\nu_{0,1}$ and β_1 this is sufficient for our purposes. We find a global optical depth at 258 GHz of 0.06. For comparison, GA12 developed a complex, 4 component model of the dust in Arp 220 including a hot component, an extended component and models for the WN and EN. They found the greatest optical depth in the WN, with $\tau_{200\mu m} = 6$–12. Assuming "worst case" parameters: $\tau_{200\mu m} = 12$ and $\beta_{WN} = 1$–2 gives $\tau_{258GHz} = 2$–0.4 and $\tau_{86GHz} = 0.7$–0.04. It seems reasonable then to assume that for our 3.5 mm observations the dust is almost entirely optically thin, although it may still be optically thick at 1.2 mm. Our optical depth is significantly lower (7–33 × lower) than that obtained by GA12 for the WN. This is probably due to our much simpler fit and averaging across both nuclei. Our lower best fit temperature (62 K cf. 90–130 K) suggests that the low optical depth, high luminosity extended dust component ($\tau_{200\mu m} = 0.17$, $T_d = 90$–40 K, diameter $\sim$650 pc $\simeq 1\farcs7$ (GA12)) could be having a significant effect upon our fit.

APPENDIX B
LINE FITTING

Since we have at least one pair of blended lines, and possibly two, we used multiple component Gaussian fits to parameterize the observed lines and to provide a handle for spectral deblending. Each of the boxes in the middle rows of Figures 2–5 presents an individual fitting, which ranged from single to up to five components. We checked that randomized starting parameters (±50%) converged to the same final fits, demonstrating that the fits are robust. The number of fitting components was chosen such that χ^2_ν was closest to unity without having consecutive residuals above $\pm 1\sigma$. The rms. uncertainty in each channel was included in the fitting.

We include below in Table 8 the details of the Gaussian fitting to the spectra. These Gaussians should not be interpreted literally as the line profiles, but rather as well defined parametric descriptions of lines' peaks and areas. Reduced χ^2 is between 0.2 and 0.7 for all fits.

Uncertainties in the fitting were derived from the covariance matrixes. For functions making use of more than one fitting parameter (such as the flux of a component or the total flux of a line summed over all components) the correlations in the covariance matrices were taken into account when calculating uncertainties.

APPENDIX C
$H^{13}CO^+$(3–2) ESTIMATION

Quantitatively, we use the HCO^+(3–2) data to estimate the predicted $H^{13}CO^+$(3–2) contribution. From Sa09 (data kindly provided by Sakamoto) we have the peak brightness temperature, optical depth and FWHM of the best fit Gaussian to the emission region of the line profile. The optical depth is found for the absorbing column, where the observed fractional absorption,

$$f_a = \frac{I_{\rm out}}{I_{\rm in}} - 1, \quad \text{(C1)}$$

gives the optical depth of the absorption component:

$$\tau_a = -\log(1 + f_a). \quad \text{(C2)}$$

Table 8
Details of Gaussian Line Fitting

WN					
Line	Component	S_v (mJy)	Center[a] (GHz)	FWHM (km s^{-1})	Area[b] (Jy km s^{-1})
SO(6_6–5_5)	1	32 ± 20	253.69	350 ± 300	12 ± 18(18)
HC^{15}N(3–2)	1	30 ± 60	253.55	230 ± 40	6 ± 15(15)
SiO(6–5)	1	39.9 ± 2.5	255.589	223 ± 23	9,5 ± 0.5(1.1)
	2	66.8 ± 3.0	255.800	153 ± 11	10.9 ± 0.9(1.4)
	3	−20.8 ± 3.8	256.000	97 ± 36	−2.1 ± 0.9(0.9)
	4	20.3 ± 4	256.099	90 ± 40	2.0 ± 1.1(1.1)
	5	−15.4 ± 2.7	256.280	190 ± 50	−3.1 ± 0.3(0.5)
H^{13}CN(3–2)	1	173 ± 19	254.304	159 ± 18	22 ± 6(6)
	2	69 ± 4	254.600	141 ± 13	10.3 ± 1.5(1.8)
	3	110 ± 15	254.433	170 ± 30	20 ± 7(7)
HN^{13}C(3–2)	1	42 ± 20	256.789	330 ± 300	15 ± 20(20)
	2	90 ± 40	256.617	240 ± 40	22 ± 18(18)
H^{13}CN(1–0)	1	12.1 ± 1.0	84.806	310 ± 30	4.0 ± 0.07(0.4)
SiO(2–1)	1	10.4 ± 0.9	85.288	410 ± 40	4.49 ± 0.12(0.5)
	2	1.5 ± 1.2	85.137	220 ± 220	0.35 ± 0.07(0.08)
EN					
Line	Component	S_v (mJy)	Center[a] (GHz)	FWHM (km s^{-1})	Area[b] (Jy km s^{-1})
SO(6_6–5_5)	1	15 ± 4	253.636	201 ± 28	3.2 ± 1.2(1.2)
HC^{15}N(3–2)	1	16.9 ± 2.3	253.460	170 ± 60	3.1 ± 1.1(1.2)
SiO(6–5)	1	12 ± 3	255.460	120 ± 40	1.63 ± 0.19(0.25)
	2	20.9 ± 2.5	255.697	220 ± 30	4.87 ± 0.19(0.5)
H^{13}CN(3–2)	1	52.0 ± 2.7	254.256	182 ± 12	10.06 ± 0.26(1.0)
	2	20 ± 3	254.463	125 ± 26	2.60 ± 0.18(0.31)
HN^{13}C(3–2)	1	23 ± 4	256.451	133 ± 27	3.2 ± 1.1(1.2)
	2	18.2 ± 2.3	256.655	270 ± 60	5.2 ± 0.6(0.8)
H^{13}CN(1–0)	1	2.6 ± 0.6	84.751	180 ± 50	0.497 ± 0.018(0.053)
SiO(2–1)	1	0.9 ± 0.5	85.165	240 ± 200	0.22 ± 0.06(0.06)
	2	3.2 ± 0.6	85.248	170 ± 40	0.56 ± 0.16(0.17)
	3	1.5 ± 0.8	85.339	90 ± 60	0.145 ± 0.013(0.019)

Notes. Errors are determined from the fitting covariance matrices.
[a] In the sky frame.
[b] Errors in parentheses include the 10% calibration error. These errors also account for the correlations between the component peaks and widths.

For an integrated line emission intensity:

$$W = \int T_{\rm B} {\rm d}v \simeq 1.064\, T_{\rm B,peak}\, v_{\rm FWHM}, \qquad \text{(C3)}$$

we have an upper level column density:

$$N_u = \frac{8\pi k \nu^2 W}{hc^3 A}\left(\frac{\Delta\Omega_a}{\Delta\Omega_s}\right)\left(\frac{\tau}{1-e^{-\tau}}\right), \qquad \text{(C4)}$$

where A is the Einstein coefficient and $\Delta\Omega_a$ and $\Delta\Omega_s$ are the beam and source sizes respectively. If we assume that [HCO$^+$]/[H^{13}CO$^+$]$\simeq$ 60, that the two isotopologues trace similar regions and share similar excitation properties then if the source sizes are the same for both isotopologues or if they are beam filling sources we have:

$$W_{13} = \frac{1}{60}\frac{\nu_{12}^2}{\nu_{13}^2}\frac{\tau_{12}}{1-e^{-\tau_{12}}}\frac{1-e^{-\tau_{13}}}{\tau_{13}} W_{12}. \qquad \text{(C5)}$$

Here the subscripts 12 and 13 refer to the H^{12}CO$^+$ and H^{13}CO$^+$ properties respectively, and ν is the frequency of the (3–2) rotational transition. For the WN peak $T_{\rm B}$ and FWHM we have $W_{12} \sim 2500$ K km s^{-1}, so with $\tau_{12} = 0.36$ and our fitted width of 180 km^{-1} to the emission region of the suspected H^{13}CO$^+$(3–2) line we have a predicted peak $T_{\rm B} = 0.27$ K $\simeq$ 2.9 mJy beam^{-1}. I.e. the peak contribution from H^{13}CO$^+$(3–2) is expected to be $\simeq 1\sigma$. It is worth noting that the HCO$^+$(3–2) and SiO(6–5) FWHMs are significantly larger (closer to 500 km s^{-1}), suggesting a lower peak, but also that the optical depth has been derived from absorption, so the true optical depth is likely larger, raising the peak. The estimate is therefore quite uncertain, but demonstrates the possibility of H^{13}CO$^+$(3–2) being seen in the WN. In the EN, Sa09 found a significantly higher HCO$^+$(3–2) effective optical depth of 3.7. This yields an H^{13}CO$^+$(3–2) peak intensity of 10.5 mJy beam^{-1} in the EN, which is readily detected, and is in fact very similar to the observed peak near the line center.

REFERENCES

Aalto, S., Spaans, M., Wiedner, M. C., & Hüttemeister, S. 2007, A&A, 464, 193
Aalto, S., Wilner, D., Spaans, M., et al. 2009, A&A, 493, 481
Bachiller, R., & Pérez Gutiérrez, M. 1997, ApJL, 487, L93
Batejat, F., Conway, J. E., Hurley, R., et al. 2011, ApJ, 740, 95
Bayet, E., Gerin, M., Phillips, T. G., & Contursi, A. 2006, A&A, 460, 467
Bayet, E., Viti, S., Williams, D. A., & Rawlings, J. M. C. 2008, ApJ, 676, 978
Bothwell, M. S., Smail, I., Chapman, S. C., et al. 2013, MNRAS, 429, 3047

Chernin, L. M., Masson, C. R., & Fuller, G. A. 1994, ApJ, 436, 741
Cicone, C., Maiolino, R., Sturm, E., et al. 2014, A&A, 562, A21
Costagliola, F., Aalto, S., Rodriguez, M. I., et al. 2011, A&A, 528, A30
Downes, D., & Eckart, A. 2007, A&A, 468, L57
Downes, D., & Solomon, P. M. 1998, ApJ, 507, 615
Eales, S. A., Wynn-Williams, C. G., & Duncan, W. D. 1989, ApJ, 339, 859
Efstathiou, G. 2000, MNRAS, 317, 697
Emerson, J. P., Clegg, P. E., Gee, G., et al. 1984, Natur, 311, 237
Engel, H., Davies, R. I., Genzel, R., et al. 2011, ApJ, 729, 58
Fabian, A. C. 2012, ARA&A, 50, 455
Ferrarese, L., & Merritt, D. 2000, ApJL, 539, L9
Fischer, J., Satyapal, S., Luhman, M. L., et al. 1997, in ESA Special Publication, Vol. 419, The first ISO workshop on Analytical Spectroscopy, ed. A. M. Heras, K. Leech, N. R. Trams, & M. Perry (Noordwijk: ESA), 149
García-Burillo, S., Combes, F., Usero, A., et al. 2014, A&A, 567, A125
García-Burillo, S., Martín-Pintado, J., Fuente, A., & Neri, R. 2000, A&A, 355, 499
García-Burillo, S., Martín-Pintado, J., Fuente, A., & Neri, R. 2001, ApJL, 563, L27
García-Burillo, S., Usero, A., Fuente, A., et al. 2010, A&A, 519, A2
González-Alfonso, E., Fischer, J., Bruderer, S., et al. 2013, A&A, 550, A25
González-Alfonso, E., Fischer, J., Sturm, E., et al. 2012, A&A, 541, A4
González-Alfonso, E., Smith, H. A., Fischer, J., & Cernicharo, J. 2004, ApJ, 613, 247
Greve, T. R., Papadopoulos, P. P., Gao, Y., & Radford, S. J. E. 2009, ApJ, 6240, 1432
Guilloteau, S., & Lucas, R. 2000, in ASP Conf. Ser. 217, Imaging at Radio through Submillimeter Wavelengths, ed. J. G. Mangum & S. J. E. Radford (San Francisco, CA: ASP), 299
Harris, G. J., Larner, F. C., Tennyson, J., et al. 2008, MNRAS, 390, 143
Harrison, C. M., Alexander, D. M., Mullaney, J. R., & Swinbank, A. M. 2014, MNRAS, 441, 3306
Högbom, J. A. 1974, A&AS, 15, 417
Imanishi, M., Nakanishi, K., & Kohno, K. 2006, AJ, 131, 2888
Imanishi, M., Nakanishi, K., Tamura, Y., & Peng, C.-H. 2009, AJ, 137, 3581
Kohno, K., Matsushita, S., Vila-Vilaró, B., et al. 2001, in ASP Conf. Ser. 249, The Central Kiloparsec of Starbursts and AGN: The La Palma Connection, ed. J. H. Knapen, J. E. Beckman, I. Shlosman, & T. J. Mahoney (San Francisco, CA: ASP), 672
Krips, M., Neri, R., García-Burillo, S., et al. 2008, ApJ, 677, 262
Langer, W. D., & Penzias, A. A. 1993, ApJ, 408, 539
Lonsdale, C. J., Farrah, D., & Smith, H. E. 2006, Ultraluminous Infrared Galaxies (Chichester, UK: Praxis)
Magorrian, J., Tremaine, S., Richstone, D., et al. 1998, AJ, 115, 2285
Mangum, J. G., Darling, J., Henkel, C., et al. 2013, ApJ, 779, 33
Martín, S., Kohno, K., Izumi, T., et al. 2014, A&A, in press (arXiv:1410.2823)
Martín, S., Krips, M., Martín-Pintado, J., et al. 2011, A&A, 527, A36
Martin-Pintado, J. 1992, A&A, 254, 315
Matsushita, S., Iono, D., Petitpas, G. R., et al. 2009, ApJ, 693, 56
McDowell, J. C., Clements, D., Lamb, S., et al. 2003, ApJ, 591, 154
Meijerink, R., & Spaans, M. 2005, A&A, 436, 397
Meijerink, R., Spaans, M., & Israel, F. P. 2007, A&A, 461, 793
Meijerink, R., Spaans, M., Loenen, A. F., & van der Werf, P. P. 2011, A&A, 525, A119
Mitchell, G. F. 1984, ApJS, 54, 81
Müller, H. S. P., Schlöder, F., Stutzki, J., & Winnewisser, G. 2005, JMoSt, 742, 215
Mundell, C., Ferruit, P., & Pedlar, A. 2001, ApJ, 560, 168
Norris, R. P. 1988, MNRAS, 230, 345
Papadopoulos, P. P. 2007, ApJ, 656, 792
Papadopoulos, P. P., van der Werf, P., Isaak, K., & Xilouris, E. M. 2010, ApJ, 715, 775
Planck Collaboration, Ade, P. A. R., Aghanim, N., et al. 2013, A&A, 571, A16
Rangwala, N., Maloney, P. R., Glenn, J., et al. 2011, ApJ, 743, 94
Remijan, A. J., Markwick-Kemper, A., & ALMA Working Group on Spectral Line Frequencies 2007, BAAS, 39, 963
Rodríguez Zaurín, J., Tadhunter, C. N., González Delgado, R. M., & Zaurín, J. R. 2008, MNRAS, 384, 875
Sakamoto, K., Aalto, S., Evans, A. S., Wiedner, M. C., & Wilner, D. J. 2010, ApJL, 725, L228
Sakamoto, K., Aalto, S., Wilner, D. J., et al. 2009, ApJL, 700, L104
Sakamoto, K., & Scoville, N. 1999, ApJ, 20, 68
Sakamoto, K., Wang, J., Wiedner, M. C., et al. 2008, ApJ, 684, 957
Salter, C. J., Ghosh, T., Catinella, B., et al. 2008, AJ, 136, 389
Sanders, D. B., & Mirabel, I. F. 1996, ARA&A, 34, 749
Scoville, N., Yun, M., & Bryant, P. 1997, ApJ, 484, 702
Scoville, N. Z., Sargent, A. I., Sanders, D. B., & Soifer, B. T. 1991, ApJL, 366, L5
Silk, J., & Rees, M. J. 1998, A&A, 331, L1
Soifer, B. T., Helou, G., Lonsdale, C. J., et al. 1984, BAAS, 16, 470
Soifer, B. T., Neugebauer, G., Matthews, K., et al. 1999, ApJ, 513, 207
Soifer, B. T., Neugebauer, G., Matthews, K., et al. 2000, AJ, 119, 509
Soifer, B. T., Sanders, D. B., Madore, B. F., et al. 1987, ApJ, 320, 238
Solomon, P. M., Downes, D., & Radford, S. J. E. 1992, ApJL, 398, L29
Tremaine, S., Gebhardt, K., Bender, R., et al. 2002, ApJ, 574, 740
Usero, A., García-Burillo, S., Martín-Pintado, J., Fuente, A., & Neri, R. 2006, A&A, 448, 457
Veilleux, S., Rupke, D. S. N., Kim, D.-C., et al. 2009, ApJS, 182, 628
Weiß, A., Downes, D., Neri, R., et al. 2007, A&A, 467, 955
Wilson, C. D., Harris, W. E., Longden, R., & Scoville, N. Z. 2006, ApJ, 641, 763
Wilson, C. D., Rangwala, N., Glenn, J., et al. 2014, ApJL, 789, L36
Wright, E. L. 2006, PASP, 118, 1711
Wright, E. L., Eisenhardt, P. R. M., Mainzer, A. K., et al. 2010, AJ, 140, 1868
Young, J. S., Kenney, J., Lord, S. D., & Schloerb, F. P. 1984, ApJL, 287, L65